

**DESIGN OF RF RECEIVER COMPONENTS FOR SPACE APPLICATIONS
USING SIGE BICMOS**

A Dissertation
Presented to
The Academic Faculty

By

Jeffrey W. Teng

In Partial Fulfillment
of the Requirements for the Degree
Master of Science in the
School of Electrical and Computer Engineering

Georgia Institute of Technology

August 2021

© Jeffrey W. Teng 2021

DESIGN OF RF RECEIVER COMPONENTS FOR SPACE APPLICATIONS USING SIGE BICMOS

Thesis committee:

Dr. John D. Cressler
Electrical and Computer Engineering
Georgia Institute of Technology

Dr. Shaolan Li
Electrical and Computer Engineering
Georgia Institute of Technology

Dr. Azadeh Ansari
Electrical and Computer Engineering
Georgia Institute of Technology

Date approved: June 23, 2021

ACKNOWLEDGMENTS

I acknowledge the SiGe team at GlobalFoundries for providing device samples. I further acknowledge the radiation effects team at Vanderbilt University for access to their testing facilities.

I would like to thank the members of my thesis committee for their time in the review of this Master's thesis. I also thank all the members of the SiGe team for their assistance.

TABLE OF CONTENTS

Acknowledgments	iii
List of Tables	vii
List of Figures	viii
List of Acronyms	xi
Summary	xiii
Chapter 1: Introduction and Background	1
1.1 Radiation Effects in SiGe BiCMOS	1
1.1.1 Ionizing-Dose Effects	1
1.1.2 Displacement-Damage Effects	3
1.1.3 Single-Event Effects	3
1.2 Ka-band Phased Arrays	3
1.3 System-Level Considerations for Space Applications	4
1.3.1 Variability in TID Response	4
1.3.2 Amplitude Control for Phased Arrays	5
1.4 Proposed Work	6
Chapter 2: Variability in the TID Response of SiGe HBTs	7

2.1	Experimental Setup and Procedure	7
2.1.1	Device Samples	7
2.1.2	Device Characterization	8
2.2	Measurement Results	9
2.3	Analysis	14
2.4	TCAD Modeling	18
2.4.1	Monte Carlo Analysis	18
2.4.2	Challenges for Predicting Post-Irradiation Performance	23
2.5	Implications for Radiation-Rich Applications	25
2.6	Summary	27
Chapter 3: Design of a Ka-Band VG-LNA for Space Applications		28
3.1	Circuit Design	28
3.1.1	Gain Control	28
3.1.2	Low-Noise Amplifier	29
3.1.3	Digital-to-Analog Converter	30
3.2	Measurement Results	31
3.2.1	Performance Comparison	35
Chapter 4: Impact of Variability on Circuit Performance		38
4.1	Current Mirrors	38
4.2	Current-Steering Digital-to-Analog Converter	39
Chapter 5: Future Work		42

Chapter 6: Conclusion	43
Appendices	44
Appendix A: Derivation of Base Current Correlation	45
References	46

LIST OF TABLES

2.1	Simulated Range of Correlation Between ΔI_B and AC Parameters	25
3.1	VG-LNA Component Values	28
3.2	Comparison of State-of-the-Art, Silicon-Based, Variable-Gain LNAs	37

LIST OF FIGURES

1.1	Cross section of a SiGe heterojunction bipolar transistor (HBT) with emitter in red, SiGe base in blue, extrinsic polysilicon base in magenta, and selectively-implanted collector (SIC) in green. The emitter-base spacer (EB-S) is the critical oxide for forward-active operation, and the regions of total ionizing dose (TID) damage are shown by yellow circles.	2
2.1	Number of valid samples as V_{BE} varies.	8
2.2	Mean (left), standard deviation (center), and coefficient of variation (right) for I_C as a function of bias for all measured doses. Observed glitches in the coefficient of variation (CoV) are caused by the ranging circuitry of the Agilent 4155.	9
2.3	Mean (left), standard deviation (center), and coefficient of variation (right) for I_B as a function of bias for selected doses.	10
2.4	Mean (left) and standard deviation (right) for I_B , normalized to their pre-irradiation values, as a function of bias for selected doses.	11
2.5	Scatter plots of post-irradiation I_B at 100 krad(SiO_2) (left) and 2 Mrad(SiO_2) (right) versus its pre-irradiation value. The lines show least-squares fits, and correlation is taken as the Pearson correlation coefficient, calculated from the best-fit line. A substantial decrease in correlation from 83% to 30% is observed.	12
2.6	Correlation coefficient between post-irradiation I_B and pre-irradiation I_B extracted across bias for all dose points.	13
2.7	I_B extracted at V_{BE} of 0.65 V, plotted across dose, for 10 selected devices. .	14
2.8	Correlation coefficient between post-irradiation I_B and pre-irradiation I_B extracted across bias for all dose points for inverse-mode operation.	15

2.9	Doping profiles for the various devices simulated, emphasizing the doping variations. The Ge profile was fixed, assuming that process control of SiGe growth is very well controlled.	19
2.10	Comparison of theoretical σ ($= \sqrt{\text{Var}}$) from Equation 2.5 with simulated data, showing excellent agreement over both V_{BE} and N_{it} . Data is normalized to $N_{it} = 0$ to highlight trends.	20
2.11	Comparison of theoretical correlation from Equation 2.7 to simulated data, showing acceptable agreement across both bias and trap density. The divergence around 0.95 V is a numerical artifact of the simulator.	21
2.12	Scatter plot of simulated I_{B0} to doping concentrations N_{de} (left) and N_{ab} (right) with corresponding best-fit line and correlation and bias point labeled.	22
2.13	Scatter plot of simulated ΔI_B at N_{it} of 10^{11} to doping concentrations N_{de} (left) and N_{ab} (right) with corresponding best-fit line and correlation and bias point labeled.	23
2.14	Increase in σ of I_B for three different spreads in doping.	24
2.15	Measured correlation of change in base current to pre-irradiation collector current showing increasing predictability.	25
2.16	Measured correlation of change in base current to pre-irradiation current gain, β , showing increasing predictability.	26
3.1	Schematic of the designed amplifier.	28
3.2	Simulated minimum noise figure and maximum available gain for the first stage as a function of V_{CB} of Q_1	29
3.3	Schematic of the integrated digital-to-analog converter (DAC).	31
3.4	Die micrograph of fabricated variable-gain low-noise amplifier (VG-LNA). The total area, including DC and radio frequency (RF) pads, is $1.50 \times 1.54 \text{ mm}^2$. The area of the low-noise amplifier (LNA) without the DAC is $1.35 \times 0.44 \text{ mm}^2$	32
3.5	DC power consumption over gain states showing variation from 12.0–17.3 mW for the LNA alone or 13.2–21.7 mW including the DAC.	32

3.6	Plots of (a) input matching and (b) small-signal gain across frequency for all 16 gain states. Both gain and matching bandwidth are maintained for all gain states. The dashed lines show the simulated result for the highest gain state.	33
3.7	(a) Gain over tune state and (b) corresponding change in gain over tune state.	34
3.8	Root-mean-square (RMS) phase error, $\Delta\phi$, across frequency with a peak of 10° near 35 GHz.	35
3.9	Noise figure (NF) across frequency for the highest gain state, < 5 dB across the bandwidth. Circles indicate measured frequencies.	35
3.10	Large-signal power sweeps for selected gain states at 26 GHz with dashed lines showing extraction of IP_{1dB} of -24 dBm.	36
4.1	Schematic of a simple current mirror (CM).	38
4.2	Monte Carlo (MC) simulations of the mirror ratio of a current mirror before and after irradiation.	39
4.3	MC simulations DAC transfer curves before (above) and after (below) irradiation.	40
4.4	MC simulations DAC differential nonlinearity (DNL) before (above) and after (below) irradiation.	41
4.5	MC simulations DAC integral nonlinearity (INL) before (above) and after (below) irradiation.	41

LIST OF ACRONYMS

BE	base-emitter
BJT	bipolar junction transistor
CB	collector-base
CBEBC	collector-base-emitter-base-collector
CM	current mirror
CoV	coefficient of variation
DAC	digital-to-analog converter
DDD	displacement-damage dose
DNL	differential nonlinearity
DSA	digital step attenuator
DT	deep trench
EB	emitter-base
EB-S	emitter-base spacer
EHP	electron-hole pair
ESD	electrostatic discharge
G/R	generation and recombination
GF	GlobalFoundries
HBT	heterojunction bipolar transistor
INL	integral nonlinearity
LNA	low-noise amplifier
LSB	least-significant bit
MC	Monte Carlo

mmW millimeter-wave

NF noise figure

QFN quad flat-pack no-lead

RF radio frequency

RMS root-mean-square

SCR space-charge region

SEE single-event effect

SET single-event transient

SIC selectively-implanted collector

STI shallow-trench isolation

TCAD transistor computer-aided design

TID total ionizing dose

VG-LNA variable-gain low-noise amplifier

VGA variable-gain amplifier

SUMMARY

A study of SiGe HBTs for use in space applications was presented. While SiGe HBTs are considered TID tolerant compared to CMOS at similar lithography nodes, experiment, analysis, and simulation have all shown that system-level susceptibilities still exist due to TID-induced mismatch between nominally matched transistors. This exaggeration of mismatch was connected to process variations such as random doping fluctuation. Potential methods to predict TID response from preirradiation performance are suggested, and system-level mitigation methods must be applied when high levels of TID are expected.

The design of a SiGe-based, space-capable VG-LNA was presented, where power and noise performance are optimized by the use of a bias-tuned topology compared to a more common LNA with digital step attenuator (DSA) combination. The designed and characterized VG-LNA demonstrates state-of-the-art performance for both noise and DC power consumption.

Future work should be focused on exposing the system-level failure mechanisms that appear when device mismatch is an error. Critical circuits and sub-circuits such as current mirrors and DACs should be examined to develop a complete understanding of issues that arise as more complex systems are considered.

CHAPTER 1

INTRODUCTION AND BACKGROUND

1.1 Radiation Effects in SiGe BiCMOS

The effects of radiation are broadly categorized into three groups: TID effects, displacement-damage dose (DDD) effects, and single-event effects (SEEs). The response of SiGe HBTs to these types of radiation has been studied since the earliest generations of SiGe BiCMOS technology platforms [1, 2]. The tolerance of SiGe HBTs to TID was shown early on [1, 3], leading to an interest in the use of SiGe HBTs for radiation-intense applications such as space exploration and particle accelerator instrumentation [4, 5]. Since then, extensive work has been conducted on SiGe HBTs and other devices in SiGe BiCMOS platforms to understand their tolerance (or intolerance) to radiation [6]. Recently, SiGe HBTs have demonstrated performance at 100s of GHz [7, 8, 9]. Accordingly, more interest has been shown for using SiGe HBTs in RF, millimeter-wave (mmW), and even sub-THz applications [10]. Thus, new emphasis has been placed on qualifying the behavior of high-frequency circuit components subject to radiation.

1.1.1 Ionizing-Dose Effects

When charged particles such as X-rays or γ -rays pass through SiO_2 , if their energy is sufficiently high, electron-hole pairs (EHPs) can be generated by direct ionization of electrons from the valence band to the conduction band. Since the mobility of electrons is much larger than that of holes in SiO_2 , the electrons tend to be swept away by electric fields, leaving fixed positive charges, which behave as traps. Over time, these positive charges can diffuse to oxide-semiconductor interfaces, becoming interface traps [11].

The locations where interface traps become critical to SiGe HBT performance in forward-

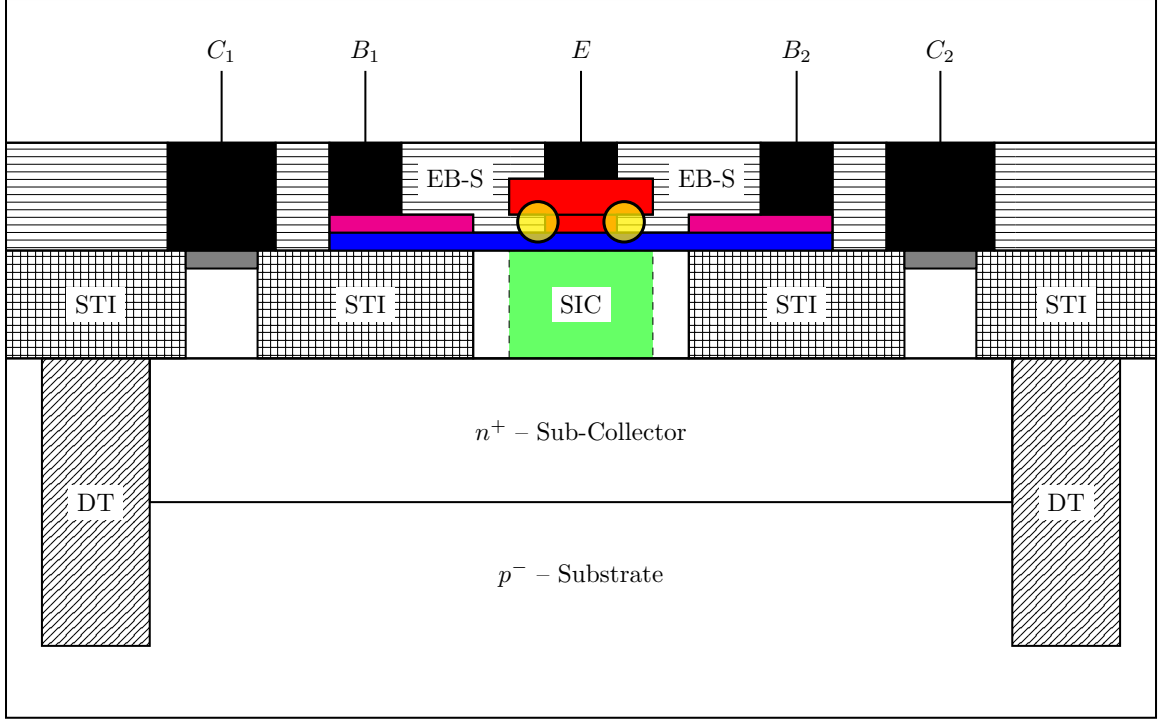


Figure 1.1: Cross section of a SiGe HBT with emitter in red, SiGe base in blue, extrinsic polysilicon base in magenta, and SiC in green. The EB-S is the critical oxide for forward-active operation, and the regions of TID damage are shown by yellow circles.

active mode are shown in Figure 1.1. Generally, after TID, interface traps are formed around the deep trench (DT) isolation oxide, the shallow-trench isolation (STI), and the EB-S oxide. However, the current distribution throughout the device desensitizes forward-active mode performance to traps in the DT and STI. The primary mechanism for forward-active collector current is the diffusion of electrons across the emitter-base (EB) junction, which traverse the quasi-neutral base region to reach the collector. This current is typically constrained to the center of the device, so the carriers are unlikely to interact with the STI/collector interface or DT/sub-collector interface. Therefore, for operation in forward-active mode (e.g., amplifiers), the EB-S is the critical oxide.

When interface traps are formed near the EB-S, they tend to increase the base leakage current due to more carrier recombination in the EB space-charge region (SCR) [1]. Correspondingly, the current gain decreases. The trapping lifetime also increases the device's flicker noise power [1]. On the other hand, only minor degradation in transistor speed has

been documented [12]. Resulting impacts on LNA and receiver performance have been studied, and mitigation methods have been proposed [13, 14]. Overall, SiGe HBTs are considered tolerant to TID up to several Mrad(SiO₂) [3, 6].

1.1.2 Displacement-Damage Effects

DDD generates bulk traps in silicon, as compared to TID, which generates mostly oxide and interface traps. The fundamental trap physics has been studied, demonstrating increased base current and decreased collector current due to bulk traps [15]. Frequency synthesizers have been shown to be sensitive to DDD effects, and damage mitigation methods have been proposed [16]. Previous work has shown SiGe HBTs to be highly tolerant to DDD due to 1-MeV neutrons [17].

1.1.3 Single-Event Effects

Although the SiGe HBT is relatively tolerant to TID and DDD effects, it remains sensitive to single-event transients (SETs), short pulses of current created by energetic particles passing through the HBT. Investigations of the impact of SETs on RF and mmW LNAs [18, 19, 20] and mixers [21] have been conducted. Correspondingly, the effects of SETs on receiver performance have been shown [22, 23]. Methods of detecting [24] and mitigating SET-induced errors in receivers have been proposed in response [25, 26, 27, 28].

1.2 Ka-band Phased Arrays

Emerging radar and communications applications have driven the development of highly integrated phased arrays. By intelligently combining radiated signals from multiple antennas in an array, the direction of maximum antenna gain can be dynamically pointed towards a desired target. Such technology is essential in orbital space applications (e.g, CubeSat and SmallSat constellations), where communications circuits need to transmit very long distances and precision imaging is necessary for scientific exploration.

Operating at higher frequency, such as at K_a -band, has gained momentum in order to improve instrument spatial resolution [29] and reduce size, weight, and power (SWaP). However, moving to K_a -band over legacy solutions at X-band and below presents design challenges in the receiver. In particular, electronic components tend to consume more power and introduce more noise as frequency increases. To support higher frequency, technology scaling leads to higher power densities, making the noise and power trade-off more stringent.

To achieve pointing with a phased array, the relative amplitudes and phases must be controlled amongst the numerous antenna elements. K_a -band arrays have been proposed, which utilize improved RF performance of modern silicon process technologies to achieve excellent performance [30, 31, 32, 33]. To further boost available phased-array performance, novel phase shifter [34, 35, 36] and attenuator [37, 38, 39] topologies have been proposed in silicon technologies for K_a -band operation.

1.3 System-Level Considerations for Space Applications

1.3.1 Variability in TID Response

SiGe HBTs are often considered tolerant to TID on the because they exhibit minimal degradation to AC performance while having nearly negligible changes DC characteristics compared to CMOS at similar lithographic nodes. However, new concerns arise at the system level, where low degradation on average is insufficient to guarantee system performance. In precision instrumentation amplifiers, for example, device-to-device matching is critical to reduce common-mode noise [40]. As another example, in data converters, device matching is a key bottleneck for both noise and linearity [41]. Ideally, when two supposedly performance-matched devices experience degradation due to TID, it is desirable that they degrade in a similar fashion as to remain matched over dose. Therefore, a comprehensive investigation of the statistics of TID response in the SiGe HBT is necessary to fully understand the ramifications of TID on important circuits like instrumentation amplifiers and

data converters.

Previous investigations have shown that, in both CMOS [42, 43, 44, 45, 46] and bipolar technologies [47, 48, 49], TID increases device-to-device and part-to-part variability. The authors in [50] give some insight into the origins of increased variability in lateral, silicon, *pn*p bipolar junction transistors (BJTs). However, since the flow of current in the SiGe HBT is vertical, the carriers' interactions with critical oxides are fundamentally different, and the existing analysis may not apply.

1.3.2 Amplitude Control for Phased Arrays

The RainCube [51] is a weather radar CubeSat operating at K_a -band. Its development emphasized the need to simultaneously reduce power consumption and improve minimum detectable reflectivity (i.e., system noise) to enable upcoming weather monitoring applications. Furthermore, these improvements should come at minimum overhead to system complexity. Many phased arrays use an LNA to maximize receiver sensitivity, then rely on DSAs to adjust the relative weights of array elements. While conceptually straightforward, the use of a DSA not only increases size and complexity, but imposes more stringent performance constraints on the LNA. To maintain receiver sensitivity at high attenuation, the LNA needs to provide high gain, therefore consume more power, to suppress the noise contribution of the DSA and overcome its reference-state insertion loss.

Since low-power, low-noise operation is essential to supporting long mission duration and accurate scientific measurement, the standard LNA and DSA methodology becomes unappealing. Instead, a more tenable approach is to combine the LNA and DSA into a single, VG-LNA. This approach requires less gain and accordingly lower power consumption, while simultaneously reducing receiver noise figure by removing an explicit attenuator.

1.4 Proposed Work

To begin, an extension of the TID tolerance of SiGe HBTs is made to the variability of TID response in chapter 2. It is shown that the variability of the HBT base current increases as TID is accumulated, and further, that this increase in base current is not easily predictable. Transistor computer-aided design (TCAD) is used to investigate the physical mechanisms driving these changes.

In chapter 3, the design of a VG-LNA targeting space applications is discussed. A comparison of variable-gain techniques is made to motivate bias-tuned topologies. A co-integrated DAC is also presented to achieve linear-in-dB gain tuning. The VG-LNA was fabricated using GlobalFoundries (GF) BiCMOS9HP technology platform, and measured performance of the fabricated VG-LNA is demonstrated, showing state-of-the-art performance among similar VG-LNAs at K_a -band.

Finally, the translation of TID-response variability to circuit and system performance is analyzed in chapter 4. CMs and current-steering DACs test vehicles to demonstrate how variability in TID response can lead to system-level degradation despite the apparent tolerance of SiGe HBTs to TID on average.

CHAPTER 2

VARIABILITY IN THE TID RESPONSE OF SIGE HBTs

2.1 Experimental Setup and Procedure

2.1.1 Device Samples

The characterized devices were fabricated in GF BiCMOS9HP, a 90-nm BiCMOS platform featuring SiGe HBTs with nominal performance reported as forward current gain $\beta = 500$, cutoff frequencies $f_T/f_{max} = 300/350$ GHz, and open-base breakdown voltage $BV_{CEO} = 1.7$ V [52]. The devices tested had a collector-base-emitter-base-collector (CBEBC) layout with an on-wafer emitter window of $0.1 \times 6.0 \mu\text{m}^2$. A schematic cross-section of this device is shown in Figure 1.1. All measured devices were taken from the same wafer lot to isolate device-to-device variation from potential lot-to-lot variation.

TID experiments were conducted at Vanderbilt University using 10-keV X-rays generated by an ARACOR Model 4100 Semiconductor Irradiation System with a dose rate of 30.26 krad(SiO₂)/min [53]. Dose rate is not expected to affect the TID response of studied SiGe HBTs [54]. Sample sets of 28 devices were wire-bonded to 100-pin quad flat-pack no-lead (QFN) packages to enable simultaneous bias and irradiation of many devices followed by rapid measurement. The QFN packages were mounted onto a test circuit board using a clamp with an aperture on top to allow X-ray exposure. Mechanical switches were used to toggle between the 28 devices. All devices in a sample set were then irradiated to 2 Mrad(SiO₂), with pauses at intermediate doses (10, 30, 50, 100, 300, 500, 1000 krad(SiO₂)) to capture any changes in DC response with increasing dose. During exposure, all terminals of all devices were grounded, which is the worst case condition for TID damage in forward-active operation [55]. Intermediate measurements were taken 5 minutes after irradiation was stopped, and the total measurement time was 40 minutes.

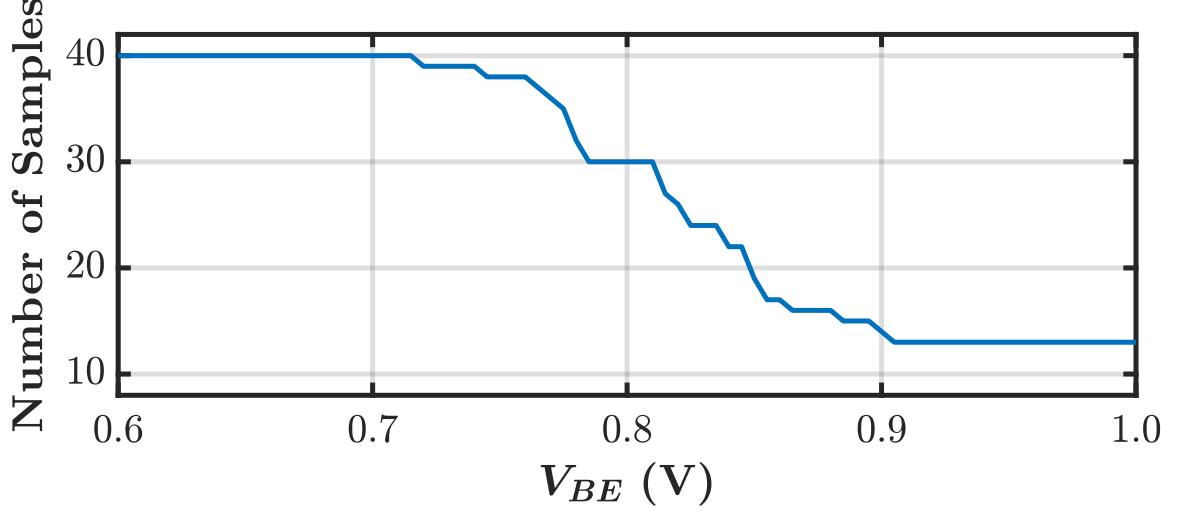


Figure 2.1: Number of valid samples as V_{BE} varies.

Temperature was monitored throughout measurement, and fluctuations within 2 °C were not significant enough to impact the results. Given the extended time required for intermediate measurements, checks for annealing were made by re-measuring the first device in the sequence after completing all 28 devices. No systematic offsets were found when re-measuring, so annealing was not considered an issue for the present study.

2.1.2 Device Characterization

The Gummel characteristics of the SiGe HBTs were used as a metrics for quantifying TID damage. The device collector current, I_C , and base current, I_B , were recorded as functions of base-emitter voltage, V_{BE} . The collector-base voltage, V_{CB} , was fixed at 0 V. Both forward- and inverse-mode characteristics were measured using an Agilent 4155 Semiconductor Parameter Analyzer.

Due to the high gain of SiGe HBTs, the devices tend to exhibit parasitic oscillatory behavior during characterization, a well-known experimental artifact [56]. The data after oscillation points are unusable, so any results at V_{BE} values higher than an oscillation point were discarded. As a result, at a given V_{BE} , the number of samples with valid data varies, as displayed in Figure 2.1. In addition, some devices demonstrated apparent degradation in

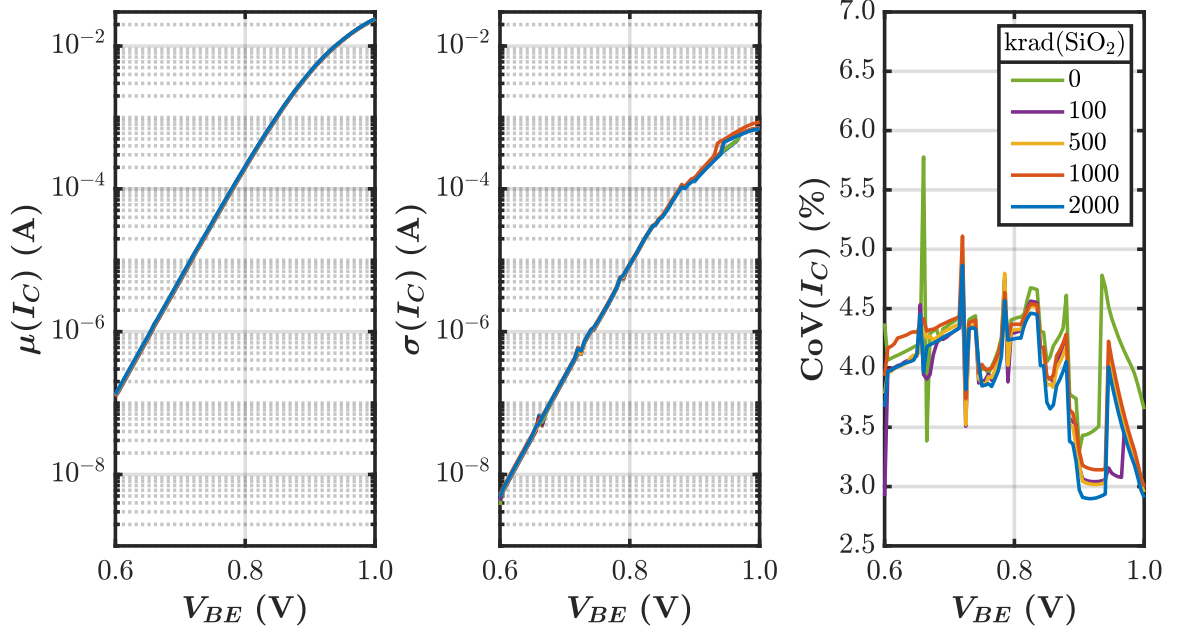


Figure 2.2: Mean (left), standard deviation (center), and coefficient of variation (right) for I_C as a function of bias for all measured doses. Observed glitches in the CoV are caused by the ranging circuitry of the Agilent 4155.

I_B consistent with electrostatic discharge (ESD) damage likely during packaging or transport. Those devices had to be omitted. While 56 devices (in two separate packages) were irradiated, only 40 could be used in statistical analysis, decreasing to 13 at high V_{BE} due to oscillations. It should be noted that the confidence in the measured statistics decreases at high V_{BE} due to the effectively smaller sample size. The decreased confidence was not a concern for the present study, since the focus was on the base current at low V_{BE} (e.g., < 0.8 V). To quantify the uncertainty in the statistics, confidence intervals for both the mean and standard deviation were calculated given the number of samples used. To achieve statistical significance with 99% confidence, any change in the mean should be more than 5% and any change in the standard deviation should be more than 40%.

2.2 Measurement Results

Statistics were calculated across the ensemble of devices. At a given TID, for each V_{BE} that was measured, the currents of all devices with valid data (sample size in Figure 2.1) were

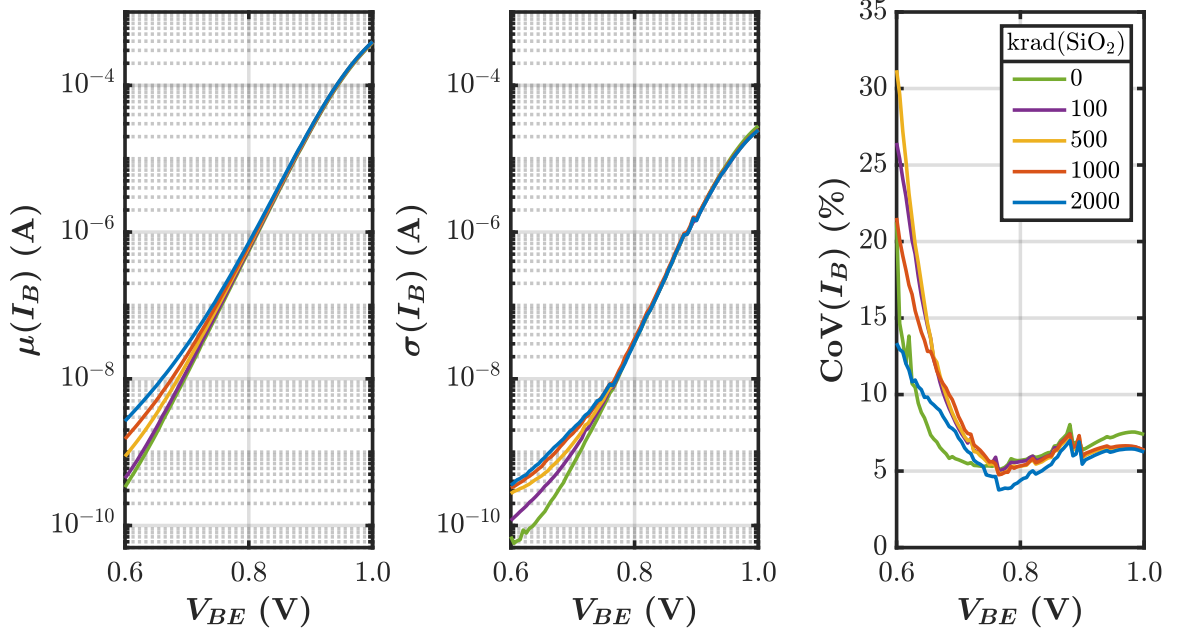


Figure 2.3: Mean (left), standard deviation (center), and coefficient of variation (right) for I_B as a function of bias for selected doses.

combined to determine the mean, μ , and standard deviation, σ . The statistics for the I_C measurements are shown in Figure 2.2 as a function of V_{BE} for all dose points. Neither the mean nor the standard deviation vary with TID, as consistent with previous literature [57, 3]. The CoV is defined as the ratio σ/μ , and measures the relative dispersion of a random variable. While standard deviation characterizes the spread of data about the mean, the CoV describes the amount by which two random samples tend to differ from each other. In cases where we wish to understand how much multiple samples deviate from a nominal performance specification, the standard deviation is most appropriate. However, for analog circuit applications where device-to-device matching is crucial, and their difference from some mean is inconsequential, such as in a DAC, the CoV is used instead of the standard deviation [58]. For example, achieving 90% yield for 12-bit DACs requires CoV less than 0.5% [58]. For I_C , the CoV changes between 3 – 5%, but does not change with dose, meaning the matching of device collector currents does not degrade with TID. Note that the measured CoV does not include special device matching techniques (e.g., common-centroid layout) and thus does not disqualify SiGe for precision DAC design. Since no

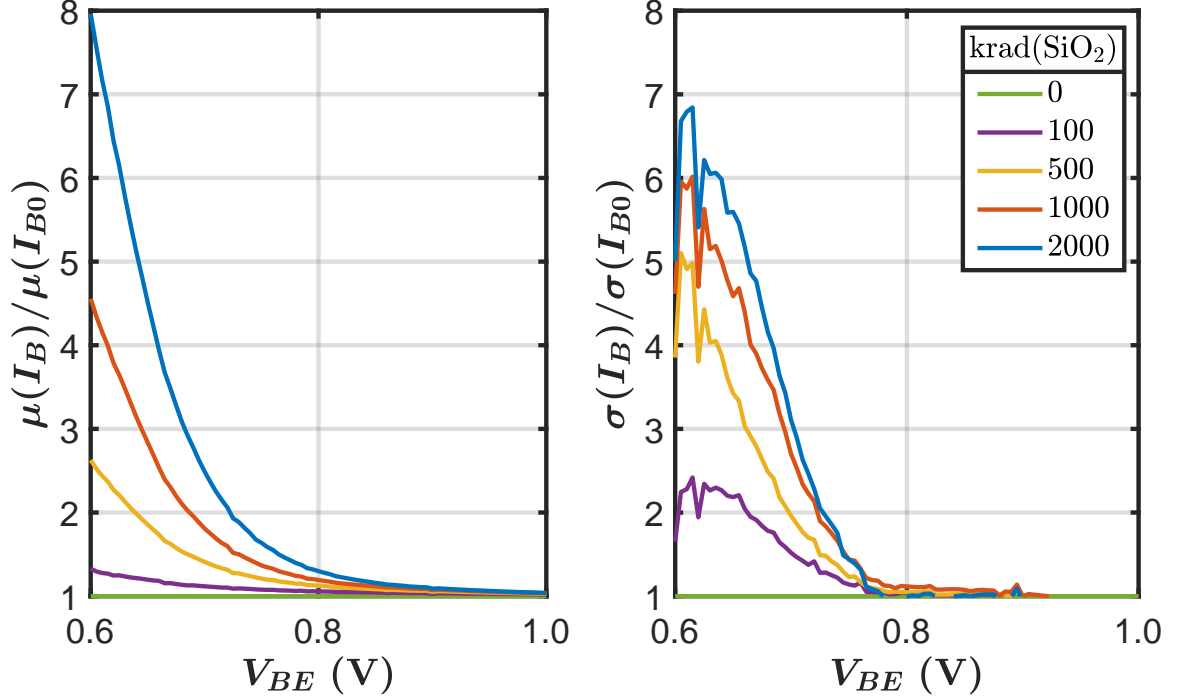


Figure 2.4: Mean (left) and standard deviation (right) for I_B , normalized to their pre-irradiation values, as a function of bias for selected doses.

statistically significant changes in I_C statistics are observed, further analysis in the present work focuses on degradation in I_B .

Figure 2.3 shows the I_B statistics as a function of V_{BE} for all dose points. The number of samples for each V_{BE} is the same as for I_C , shown in Figure 2.1. To highlight the changes, mean and standard deviation are shown again in Figure 2.4, this time normalized to their pre-irradiation values. Since the changes in μ and σ exceed 5% and 40%, respectively, these variations with TID are statistically significant. With larger dose, both the mean and standard deviation increase at low V_{BE} . It is widely known that, as TID creates traps near the EB space-charge region, trap-assisted recombination causes the average base current to increase [59, 60, 3]. However, the mechanism behind the observed increase in standard deviation is not clear, and is investigated in Section section 2.3.

The CoV for the base current is also shown in Figure 2.3. It demonstrates a non-monotonic trend over TID, peaking to 31% at 500 krad(SiO₂). This may be a concern for differential amplifiers, where mismatch in the base currents of the two input transistors can

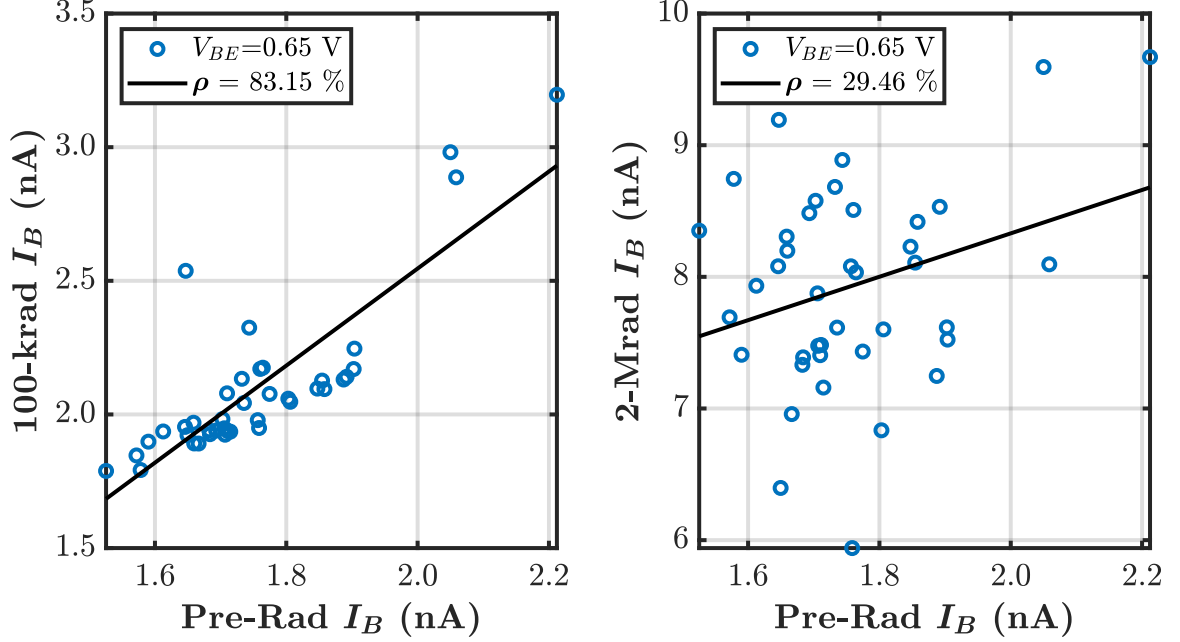


Figure 2.5: Scatter plots of post-irradiation I_B at 100 krad(SiO_2) (left) and 2 Mrad(SiO_2) (right) versus its pre-irradiation value. The lines show least-squares fits, and correlation is taken as the Pearson correlation coefficient, calculated from the best-fit line. A substantial decrease in correlation from 83% to 30% is observed.

lead to higher noise and degraded bandwidth [40].

Given that the standard deviation of I_B steadily increases as dose is accumulated, a question arises of whether the change in I_B remains predictable, which aids in both RHA testing and component selection. Therefore, is relevant to investigate the correlation coefficient, ρ , between pre-irradiation and post-irradiation device performance. The peak pre-irradiation current gain had a sample mean of 480 at V_{BE} of 0.65 V, so this bias was selected as an example for subsequent analysis. Figure 2.5 shows scatter plots of the I_B measured at 100 krad(SiO_2) and 2 Mrad(SiO_2) versus its pre-irradiation value, extracted at a V_{BE} of 0.65 V. Least-squares regression lines are superimposed, and correlation coefficient is taken from the fit. At the lower dose, the correlation is 83%, still relatively high. However, at 2 Mrad(SiO_2), the correlation decreases to 30%.

The scatter plots in Figure 2.5 were generated for all V_{BE} at each dose, and the correlation coefficients from the best-fit lines were recorded and plotted in Figure 2.6. The

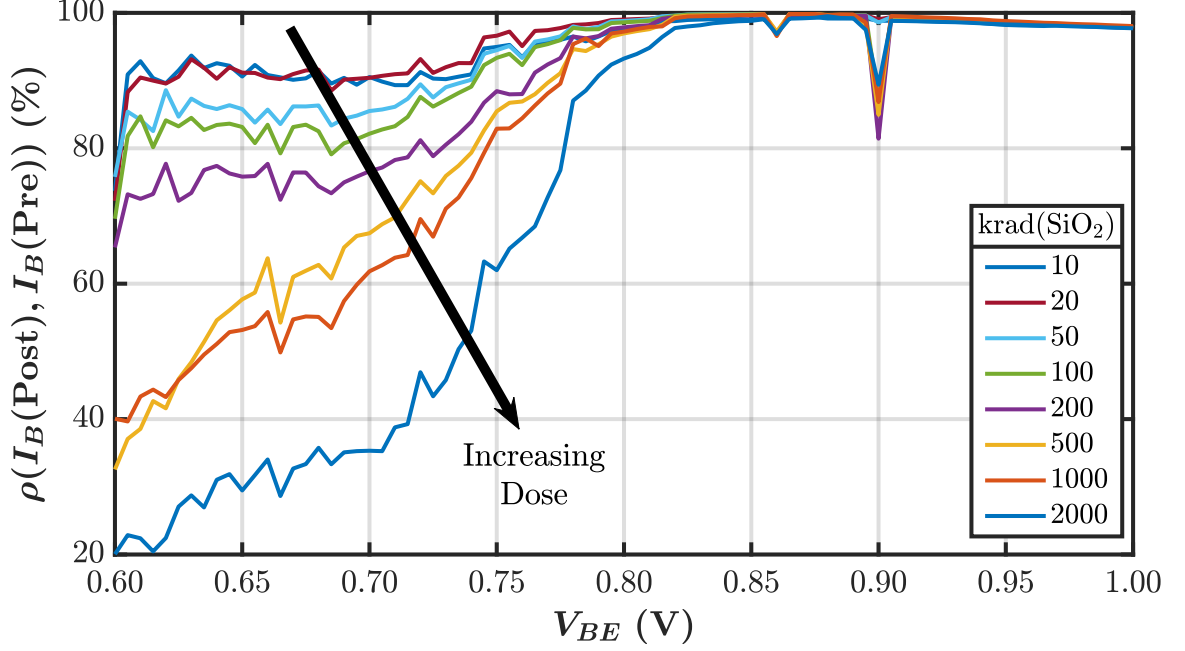


Figure 2.6: Correlation coefficient between post-irradiation I_B and pre-irradiation I_B extracted across bias for all dose points.

correlation coefficient shows a trend of decreasing correlation with increasing dose for a given bias. From Figure 2.3, base current is shown not to change significantly due to TID above V_{BE} of 0.8 V. At biases above 0.8 V, where damage is not apparent, correlation remains large. Below 0.8 V, where base-current leakage increases significantly, correlation decreases. This decrease suggests that trap-assisted generation/recombination current (post-irradiation) is independent of the diffusion current (ideal, pre-irradiation), which will be important for the analysis in Section section 2.3.

Decreasing correlation also suggests that the device performance metrics may “cross over” with increasing dose. Indeed, this behavior is present in the data in Figure 2.7. Though I_B is monotonically increasing for all devices, the slope of the increase varies, causing the curves to cross. As a result, pre-irradiation I_B is a poor predictor of post-irradiation I_B .

Since operation in inverse mode, with emitter and collector terminals swapped, has been proposed as a radiation-hardening-by-design technique [25, 26], statistics were also

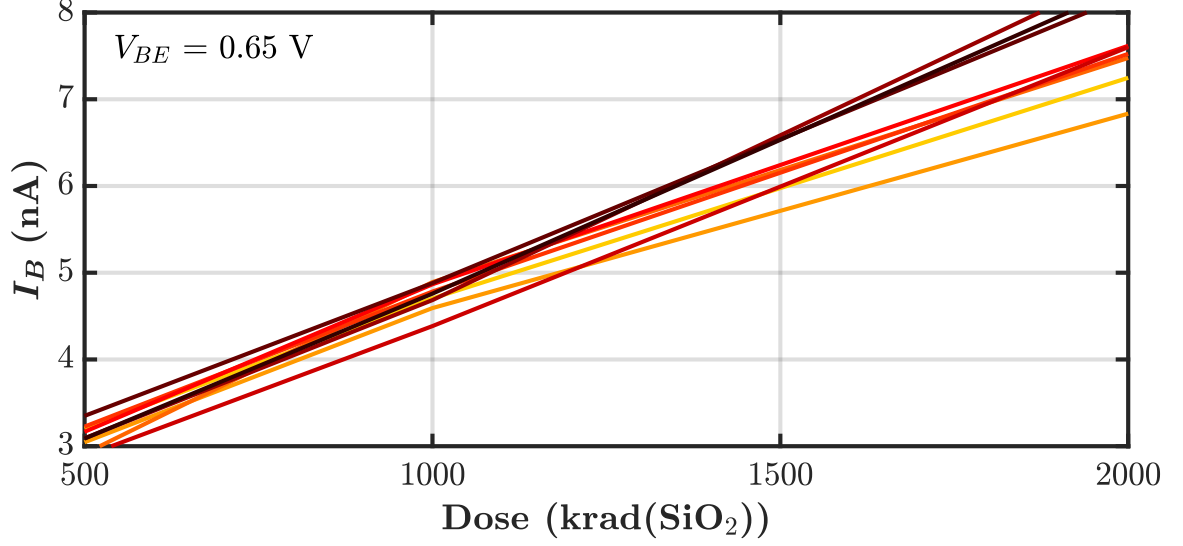


Figure 2.7: I_B extracted at V_{BE} of 0.65 V, plotted across dose, for 10 selected devices.

calculated for inverse-mode operation. Mean and standard deviation were found to increase in a similar fashion to forward mode. The correlation is shown in Figure 2.8. Indeed, inverse-mode operation still shows decreasing correlation. Thus, inverse mode does not give a benefit over forward mode for variability or predictability in TID response, yet still incurs a performance penalty, a poor trade-off for applications with high TID requirements.

2.3 Analysis

Thus far, the data have shown that TID causes increasing standard deviation and decreasing predictability in I_B . In this section, a mathematical formulation is developed for TID-response variability. These analyses will be verified in TCAD simulation. To begin, we must understand the basic operation of the SiGe HBT.

In an *npn* SiGe HBT, the ideal, pre-irradiation terminal currents originate from the drift-diffusion of carriers across the EB junction. This action is controlled by the germanium fraction at the metallurgical EB junction, x_0 , the change in the germanium fraction across the base, Δx , the metallurgical base width, W_b , and the dopant concentrations in the intrinsic emitter, N_{de} , and base, N_{ab} . Variation in the forward-mode terminal currents are dominated by these five parameters [57]. The germanium in the SiGe base is added

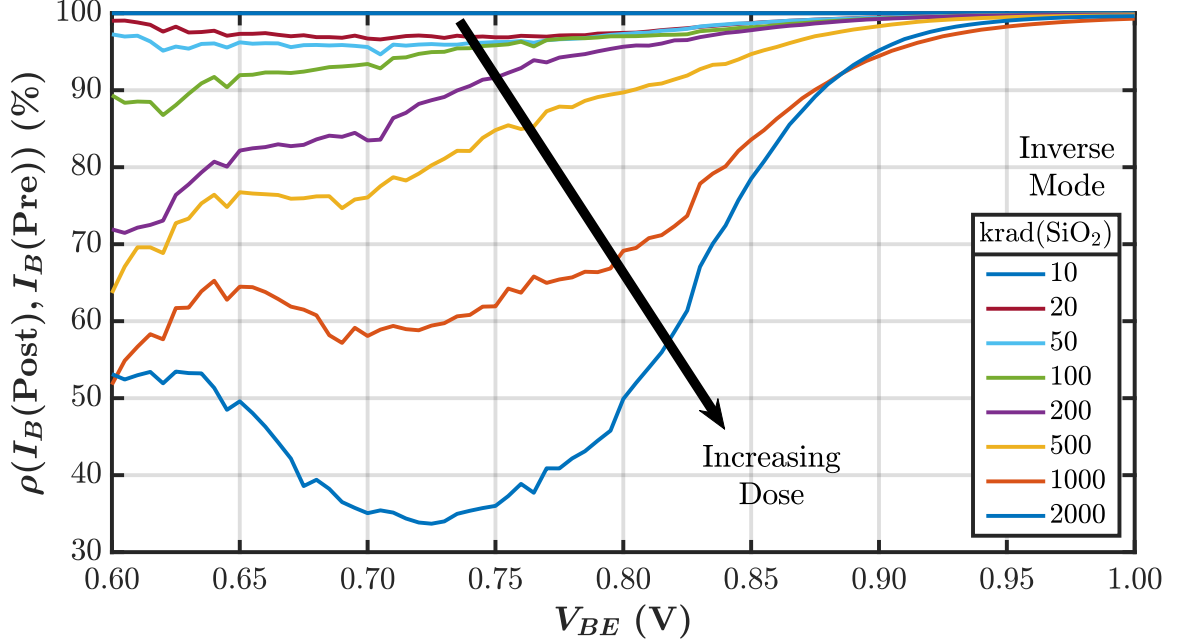


Figure 2.8: Correlation coefficient between post-irradiation I_B and pre-irradiation I_B extracted across bias for all dose points for inverse-mode operation.

during epitaxial growth, and is therefore extremely well controlled [57]. Pre-irradiation device-to-device variability, thus, should come primarily from random variation in doping concentration between devices.

Post-irradiation increases in base current arise from trap-assisted generation and recombination (G/R) due to a non-zero interface-trap density, N_{it} , generated by TID [60]. On the time scale of a DC measurement, as the Gummel characteristics in the present study, border traps are expected to behave similarly to interface traps [61, 62]. In an $nnpn$ transistor, oxide traps tend to enhance the effect of interface traps [60]. Accordingly, the behaviors of both oxide and border traps are expected to be captured by N_{it} . The translation from TID to N_{it} is determined by the electric field at the oxide-semiconductor boundary, which influences charge yield [53, 63]. Even under process variation, the electric field is not expected to be different enough to create large variations in N_{it} between devices [53]. Thus, for the present analysis, N_{it} is assumed to be constant between devices, which is sufficient to predict the behavior observed in the measured data. Under these assumptions, the variability of the base current can be examined.

In practice, I_B has a complicated dependence upon the listed parameters. To reach an intuitive explanation, it is helpful to abstract that complexity. Accordingly, let g be some function that controls the drift-diffusion component of base current, typically represented by the reverse-saturation current [64]. Additionally, let h be some function controlling the G/R component of base current, a treatment of which is presented in [60]. Note g and h are implicit functions of W_b , N_{ab} , and N_{de} and are assumed not to change with N_{it} or V_{BE} . The authors in [59] and [60] show that the G/R component is linearly proportional to the interface trap density, so N_{it} can be written explicitly, and I_B for a given device is

$$I_B = g e^{qV_{BE}/kT} + N_{it} h e^{qV_{BE}/2kT} \quad (2.1)$$

where q is the magnitude of the electron charge, k is the Boltzmann constant, and T is the device temperature. The population mean of I_B is readily determined from Equation 2.1 as

$$\mu[I_B] = \mu[g] e^{qV_{BE}/kT} + N_{it} \mu[h] e^{qV_{BE}/2kT} \quad (2.2)$$

With an expression for I_B in hand, we first investigate why σ increases in Figure 2.3. The population variance of the linear combination of two arbitrary random variables X and Y is defined to be

$$\text{Var}[aX + bY] = a^2 \text{Var}[X] + b^2 \text{Var}[Y] + 2ab \text{C}[X, Y] \quad (2.3)$$

where $\text{Var}[X]$ is the square of the standard deviation, σ^2 , of X , $\text{C}[X, Y]$ is the covariance between X and Y , and a and b are deterministic constants. In Equation 2.1, g and h are the random variables. Accordingly, the population variance of I_B as a function of V_{BE} is

$$\text{Var}[I_B] = \text{Var}[g] e^{2qV_{BE}/kT} + N_{it}^2 \text{Var}[h] e^{qV_{BE}/kT} + 2N_{it} \text{C}[g, h] e^{3qV_{BE}/2kT} \quad (2.4)$$

Examining Figure 2.6 note that the correlation coefficient decreases at low V_{BE} where the

post-irradiation I_B is predominantly G/R current. Accordingly, the correlation coefficient at low V_{BE} describes the relationship between drift-diffusion current (pre-irradiation) and G/R current (post-irradiation), which is shown to be weak. Therefore, it is assumed that $C[g, h]$ is negligible. This assumption is verified in TCAD simulation below. Under this assumption, the variance of I_B is given approximately by

$$\text{Var}[I_B] \approx \text{Var}[g]e^{2qV_{BE}/kT} + N_{it}^2 \text{Var}[h]e^{qV_{BE}/kT} \quad (2.5)$$

Recall that g and h represent process variation due to unavoidable randomness in the doping profile and do not change with V_{BE} or N_{it} . Therefore, Equation 2.5 directly reveals that the introduction of interface traps can exacerbate inherent variability, explaining the increasing σ shown in Figure 2.3. We note that these results give an optimistic bound for variability. This simplified analysis assumes N_{it} does not vary between devices, i.e., that the charge yield is the same for all measured devices. However, if this assumption is lifted, or N_{it} varies between devices due to changes in charge yield, the increase in variability can only become worse.

With the variance determined, we now examine the changes in correlation in Figure 2.6. The correlation coefficient, ρ , between random variables X and Y is defined as

$$\rho[X, Y] = \frac{C[X, Y]}{\sigma[X]\sigma[Y]} \quad (2.6)$$

Letting X be the pre-irradiation I_B ($N_{it} = 0$) and Y be the post-irradiation I_B , based on Eqs. Equation 2.1 and Equation 2.5, the pre-to-post correlation coefficient, ρ , is

$$\rho[\text{Pre}, \text{Post}] \approx \frac{\sigma[g]}{\sqrt{\text{Var}[g] + N_{it}^2 \text{Var}[h]e^{-qV_{BE}/kT}}} \quad (2.7)$$

where, again, $C[g, h]$ is assumed negligible. The full derivation is shown in Appendix A. For fixed V_{BE} Equation 2.7 predicts that the correlation will decrease from an initial value

of 100% as N_{it} increases, consistent with the data in Figure 2.6. In addition, increasing V_{BE} decreases the contribution of the N_{it} term, also reflected in Figure 2.6.

The result in Equation 2.7 shows that, regardless of the initial process variation (g and h), the predictability of the base current will always degrade as N_{it} increases, for fixed bias. This conclusion means that biasing at very low V_{BE} , for instance, to save power, will unavoidably cause the post-irradiation response to be unpredictable. In the design of a radiation-tolerant system, it is therefore desirable to determine a V_{BE} point that can optimize power and circuit performance while maintaining acceptable levels of correlation, which will depend on the maximum required operational dose.

2.4 TCAD Modeling

2.4.1 Monte Carlo Analysis

Three trends were observed with increasing dose in the analysis of section 2.3:

- Increasing μ
- Increasing σ
- Decreasing pre-irradiation to post-irradiation ρ

To provide additional insight, the device in Figure 1.1 was simulated in two dimensions using Sentaurus TCAD. The germanium profile was taken as a triangle with $x_0 = 5\%$ and $\Delta x = 20\%$. The doping concentrations were set to N_{de} of $3 \times 10^{20}/\text{cm}^3$ and N_{ab} of $5 \times 10^{19}/\text{cm}^3$. Although these parameters do not exactly represent the fabricated device, the simulations are sufficient for drawing a qualitative understanding of our observations. TID response was simulated by adding interface donor traps in the sensitive oxides, highlighted in the yellow regions of Figure 1.1. Donor traps were defined with uniform spatial distribution throughout the oxide-semiconductor interfaces and mid-bandgap energy level, with concentrations up to $10^{11}/\text{cm}^2$. Acceptor traps were determined in simulation to have insignificant effect on the base current.

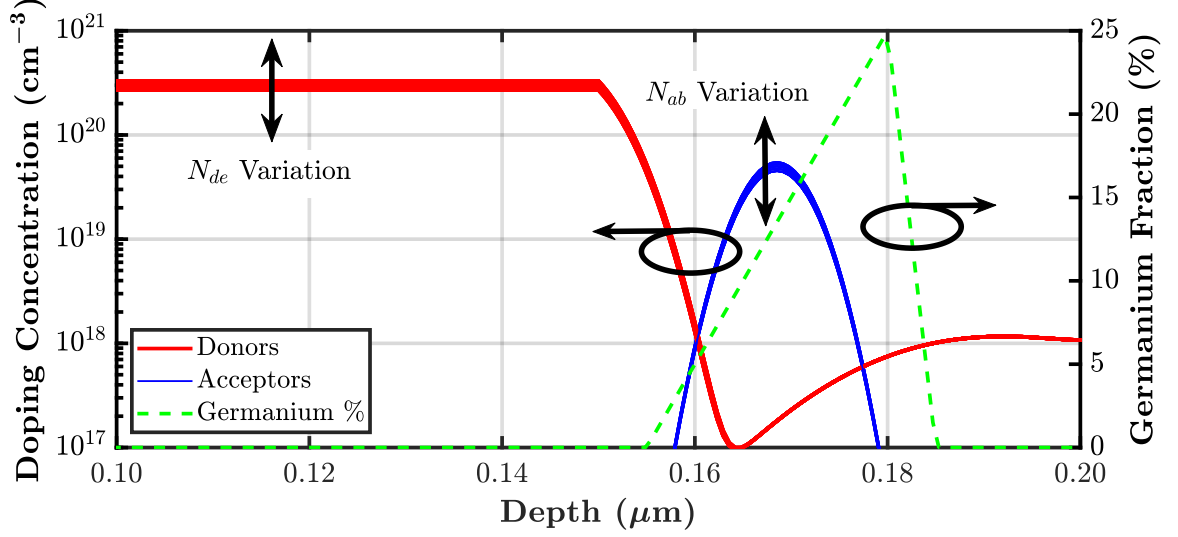


Figure 2.9: Doping profiles for the various devices simulated, emphasizing the doping variations. The Ge profile was fixed, assuming that process control of SiGe growth is very well controlled.

To simulate the randomness of doping concentrations, 40 random profiles were generated by sampling 40 values of N_{de} , 40 values of N_{ab} , and 40 values of W_b from independent Gaussian distributions, which are commonly used to model process variation [65]. Dopants are typically introduced during epitaxial growth, so variations in doping concentration come from uncertainty in the injected dopant flux [65] and the out-diffusion of dopant ions during subsequent thermal cycling [57], so we do not expect variation in the location of peak doping. Therefore, the randomness was introduced by modifying the peak and spatial distribution of the doping concentrations. Since the foundry process control specifications list 10% for emitter and base resistances, each spread in doping was taken to be 10% of the nominal peak doping concentrations given that doping and resistance are closely related [64]. The various profiles are represented in Figure 2.9 with arrows denoting where randomness was introduced.

First, consider σ as N_{it} increases. The initial I_B and the change in I_B , based on Equation 2.1, are

$$I_{B0} = I_B(N_{it} = 0) = g e^{qV_{BE}/kT} \quad (2.8)$$

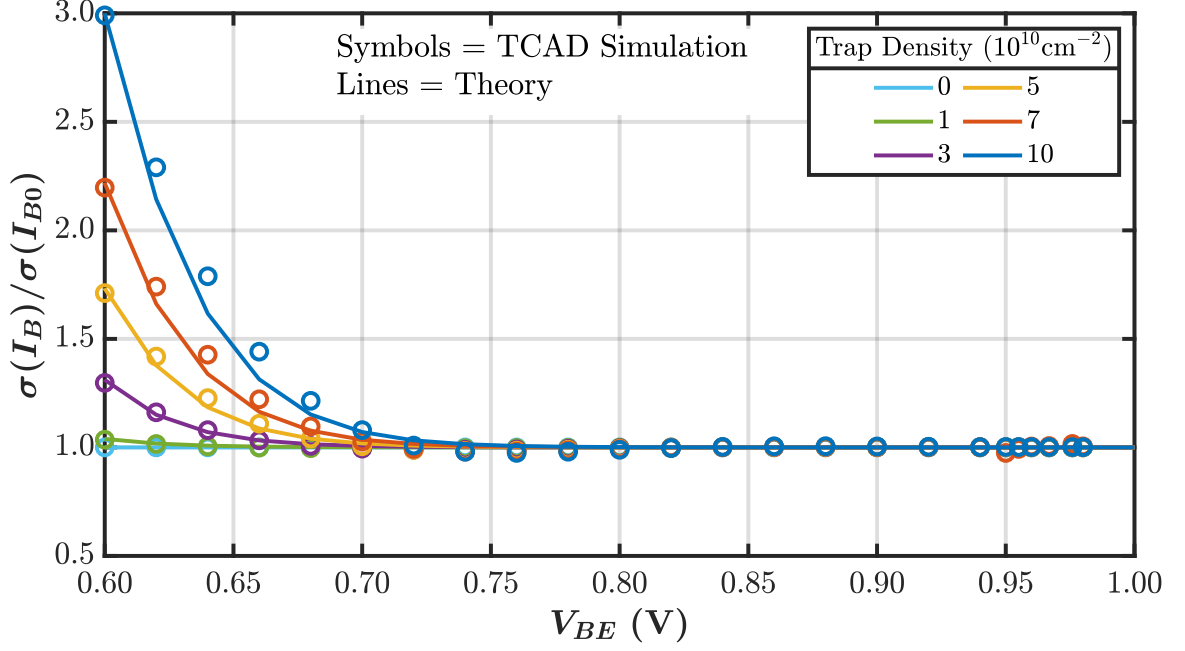


Figure 2.10: Comparison of theoretical σ ($= \sqrt{\text{Var}}$) from Equation 2.5 with simulated data, showing excellent agreement over both V_{BE} and N_{it} . Data is normalized to $N_{it} = 0$ to highlight trends.

$$\Delta I_B = I_B - I_{B0} = N_{it} h e^{qV_{BE}/2kT} \quad (2.9)$$

respectively. In simulation, N_{it} is known, so Eqs. Equation 2.8 and Equation 2.9 can be used to determine g and h . From each of the 40 simulated profiles, g and h were calculated and used to predict σ based on Equation 2.5. The results are plotted in Figure 2.10. To accentuate the trends, statistics are shown normalized to their trap-free value, similarly to the measured data in Figure 2.4. The simulations are able to reproduce the trends observed in measurement wherein σ grows for a given V_{BE} as dose (i.e., trap density) is accumulated. Further σ is shown to have excellent agreement between simulated I_B and theoretical predictions, validating our previous conclusion that TID-induced interface-trap density can exacerbate pre-existing process variation, even if N_{it} itself is the same between all devices.

Figure 2.11 compares the analytical model for the correlation of pre-to-post-irradiation base current developed in Section section 2.3 with simulation results. In Section sec-

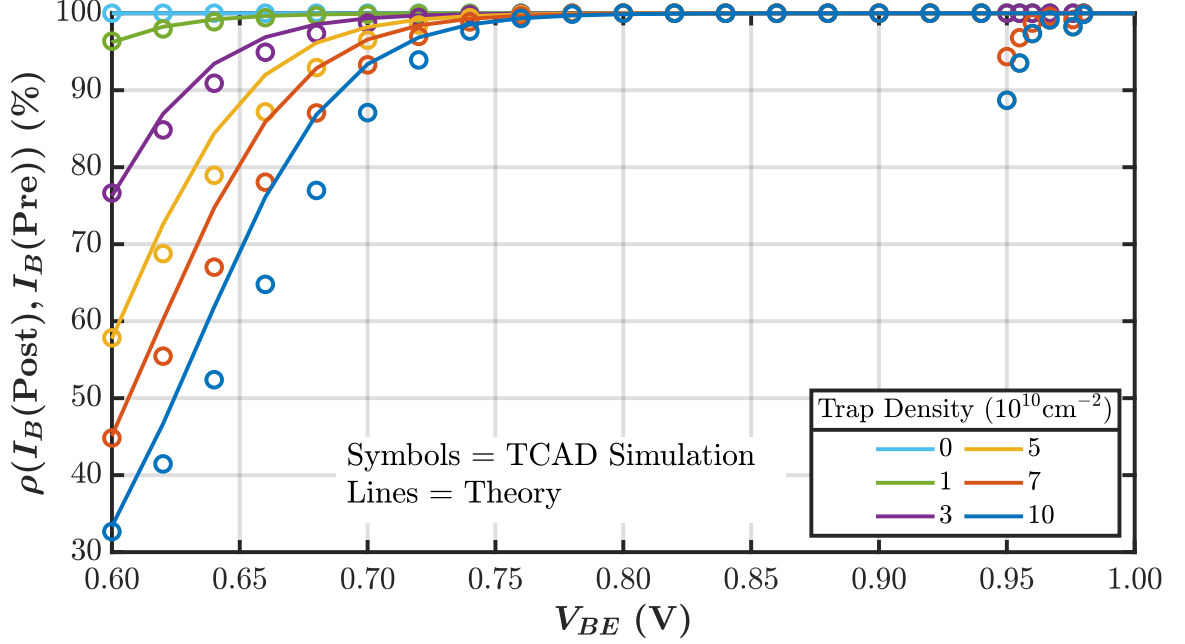


Figure 2.11: Comparison of theoretical correlation from Equation 2.7 to simulated data, showing acceptable agreement across both bias and trap density. The divergence around 0.95 V is a numerical artifact of the simulator.

tion 2.3, it was assumed that g and h do not change with N_{it} , which may not be true in real devices. Given this assumption, the result still shows reasonable agreement between simulation and theory and sufficiently captures the trends of correlation across both N_{it} and V_{BE} .

To understand why the pre-to-post correlation decreases, correlations of I_B to N_{de} and N_{ab} are examined to determine the dominant factors contributing to randomness in current. It is well known that the drift-diffusion component of I_B in a bipolar transistor is controlled primarily by its emitter doping concentration [64]. Thus, it is expected that I_{B0} is highly correlated to N_{de} and less so to N_{ab} . The simulated data are shown in Figure 2.12, corroborating the simple theory in [64].

The theory in [59, 60] demonstrates that the G/R component of post-irradiation I_B depends primarily on the base profile. This dependence is a result of the design of a bipolar transistor, where $N_{de} \gg N_{ab}$ to improve current gain, causing the interaction of carriers with interface traps to occur primarily on the base side of the emitter-base junction. To

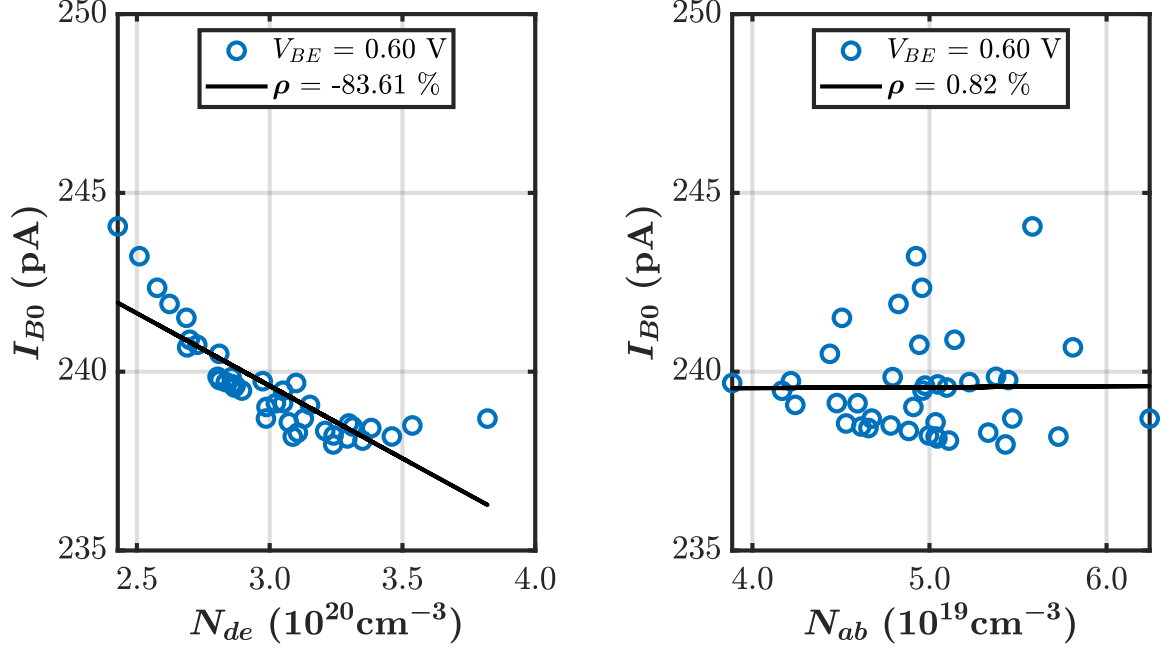


Figure 2.12: Scatter plot of simulated I_{B0} to doping concentrations N_{de} (left) and N_{ab} (right) with corresponding best-fit line and correlation and bias point labeled.

confirm this analysis, scatter plots of ΔI_B versus N_{de} and N_{ab} are shown in Figure 2.13. Indeed, the G/R component given by ΔI_B shows very little dependence on N_{de} and nearly one-to-one correspondence with N_{ab} .

The results in Figure 2.11 clearly show that ρ decreases as N_{it} rises. Then, based on Figure 2.12 and Figure 2.13, when TID is accumulated, the factors controlling I_B trade dominance between the emitter and base profiles. This trade of dominance explains why the pre-irradiation I_B is a poor predictor of the post-irradiation I_B : they are controlled by different parts of the device. Going back to the analysis in Section 2.3, this confirms our assumption that the drift-diffusion part of the current (g) and the G/R part of the current (h) are independent of each other, or that $C[g, h] \approx 0$.

Finally, the simulations were performed again with doping spreads of 5% and 1% to assess the translation from doping variation to I_B variation. The previous conclusions suggest that controlling process variation will naturally reduce post-irradiation variability. The values of σ extracted from simulation are shown in Figure 2.14 as a function of N_{it} for different doping variability. The simulated data confirm that minimizing the process

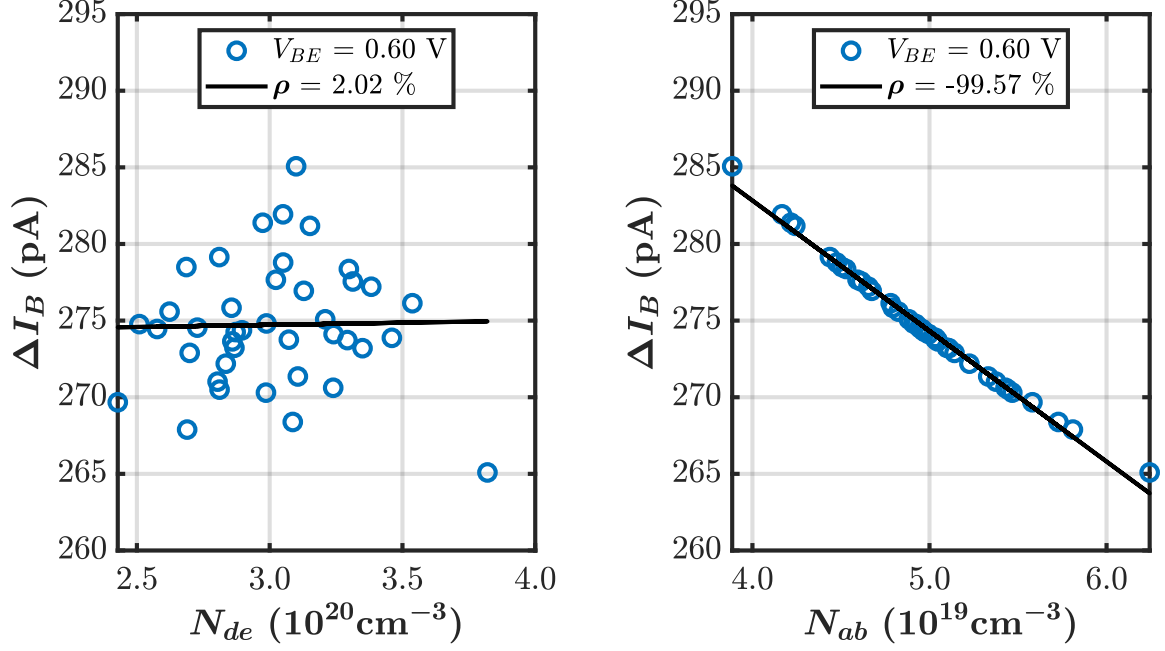


Figure 2.13: Scatter plot of simulated ΔI_B at N_{it} of 10^{11} to doping concentrations N_{de} (left) and N_{ab} (right) with corresponding best-fit line and correlation and bias point labeled.

variation, particularly in the base profile, naturally improves the post-irradiation spread.

2.4.2 Challenges for Predicting Post-Irradiation Performance

With very little correlation between pre-irradiation I_B and post-irradiation I_B , a question arises naturally: Is there any method to predict the post-irradiation I_B ? The answer to this question is critical in part selection for radiation-rich applications. If g and h were known, it would be possible to make predictions based on Equation 2.1. However, based on terminal currents only, it is difficult for a user to determine the likely post-irradiation N_{it} . A possible approach is to fit the mean data in Figure 2.3 to Equation 2.2. However, it remains difficult to determine N_{it} without prior knowledge of h or some external way to determine it. Previous work suggests a sophisticated method to extract N_{it} in silicon BJTs [59, 60], but the introduction of Ge to the base complicates the problem.

Instead, we found that other device performance metrics that are controlled by N_{ab} , which also controls ΔI_B , serve as better predictors of post-irradiation base current. For instance, the collector current, I_C , is known to be controlled primarily by the base profile [57,

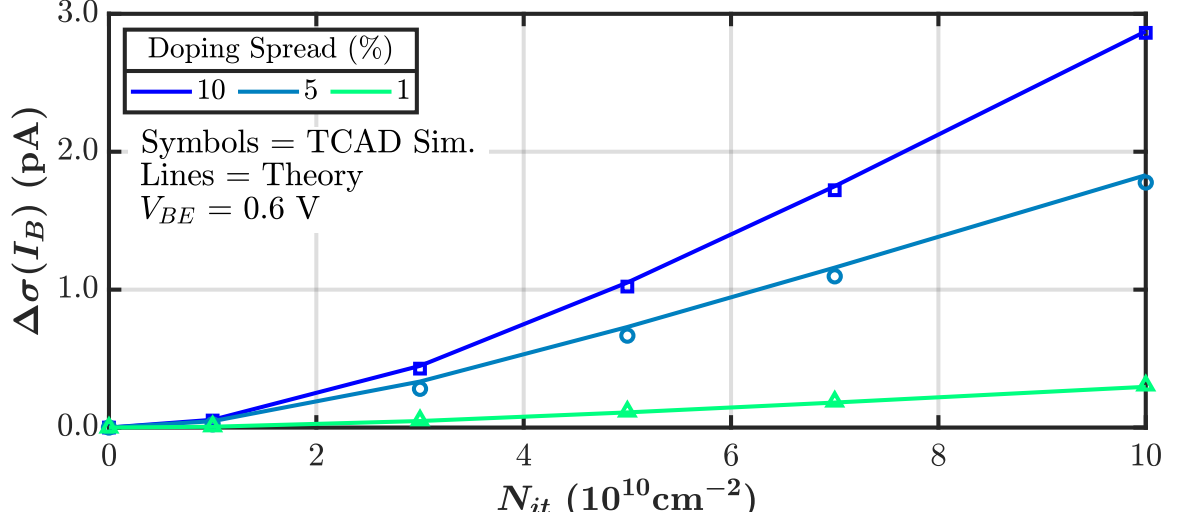


Figure 2.14: Increase in σ of I_B for three different spreads in doping.

64]. Unfortunately, this idealized behavior does not translate perfectly to measured data, as shown in Figure 2.15. An ideal predictor would be close to 100% correlated with the ΔI_B such that the post-irradiation spread in base current is completely captured. Indeed, I_C shows some correlation to ΔI_B , but not enough to be used as a sole predictor of post-irradiation performance, only capturing around 50% of the post-irradiation I_B at best.

To further explore this suggested predictive method, various combinations of the measured I_B and I_C were tested as predictors of either post-irradiation I_B or ΔI_B . A promising example was ΔI_B and pre-irradiation current gain, β . The data are shown in Figure 2.16, where correlation between pre-irradiation β and post-irradiation ΔI_B increases to a peak of 75% at the highest dose.

Although AC small-signal parameters could not be measured in the experimental setup for the present study, TCAD simulations could be used as a preliminary test to identify potential AC predictors of TID response. From the same 40 devices simulated in Section section 2.4, collector-base (CB) capacitance, C_{CB} , base-emitter (BE) capacitance, C_{BE} , and base resistance, R_B , were extracted from two-port network parameters [66]. Their correlations with ΔI_B are listed in Table 2.1. The listed ranges were determined across all N_{it} and V_{BE} values. R_B shows a very high correlation with ΔI_B , meaning a linear fit of ΔI_B

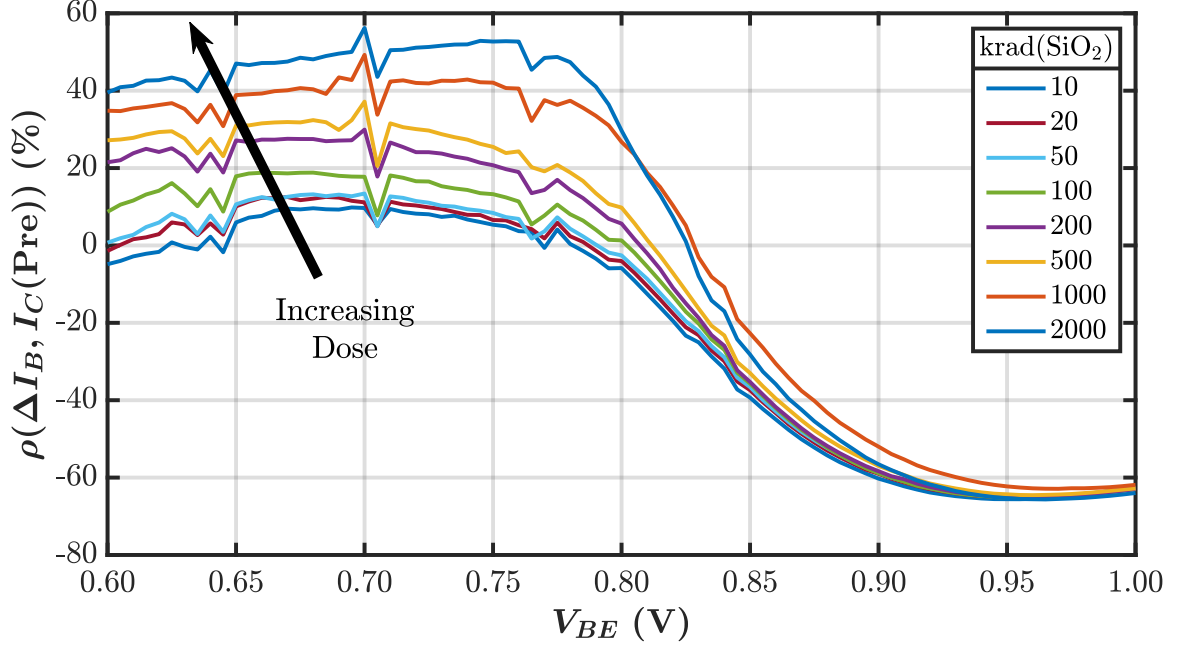


Figure 2.15: Measured correlation of change in base current to pre-irradiation collector current showing increasing predictability.

Table 2.1: Simulated Range of Correlation Between ΔI_B and AC Parameters

Parameter	Correlation with ΔI_B (%)
C_{BE}	$(-70, -80)$
C_{CB}	$(-10, +10)$
R_B	$(+90, +99)$

as a function of R_B captures at least 90% of the spread in ΔI_B . While R_B seems to be an excellent predictor, this simulated result needs further testing in measurement.

2.5 Implications for Radiation-Rich Applications

Three major trends over dose can be observed from the data. As dose is increased:

1. the mean I_B increases (as expected)
2. the standard deviation of I_B increases
3. the correlation of pre-irradiation I_B to post-irradiation I_B decreases.

Result 1) is important for low-power circuitry, where a device might have quiescent bias

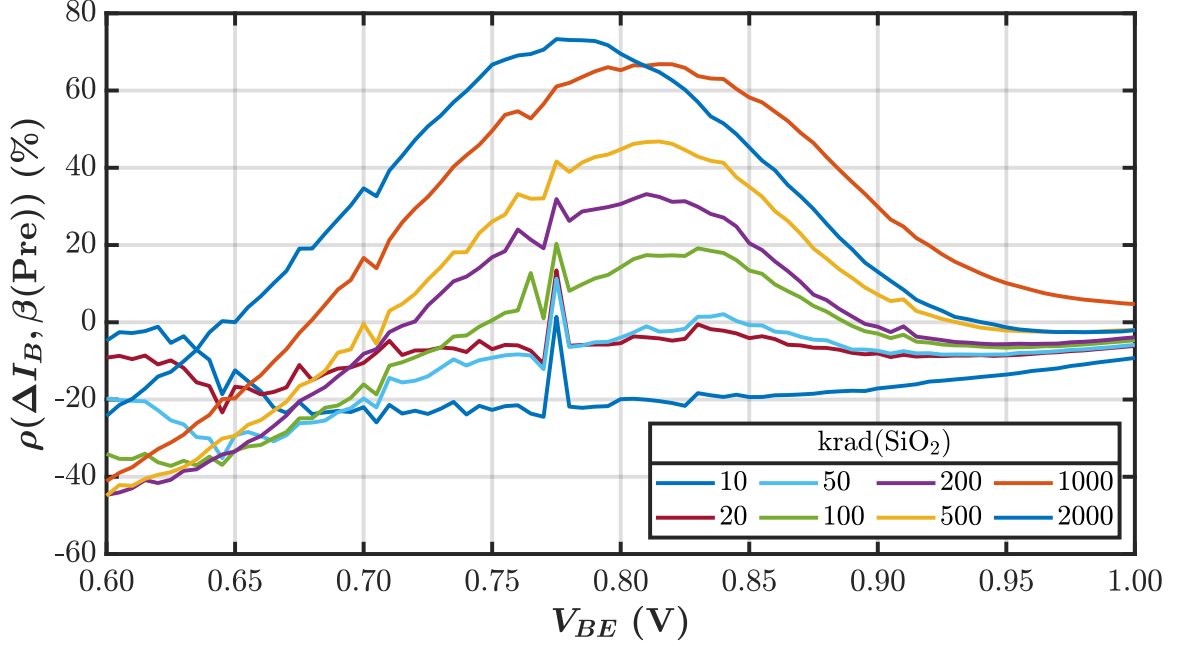


Figure 2.16: Measured correlation of change in base current to pre-irradiation current gain, β , showing increasing predictability.

at a V_{BE} where I_B degrades. For instance, in an operational amplifier, increased I_B causes the input impedance of the amplifier to drop, lowering the loaded voltage gain as dose accumulates. When also considering 2), the problem becomes worse. Variation between amplifiers can generate offset voltages in the signal path. Since standard deviation is rising, those offset voltages are expected to rise as well. Such offsets can lead to degraded dynamic range. In the worst case, offset can saturate receiver channels, rendering them inoperable.

Trend 3) is problematic for component selection and RHA testing. One might naively choose parts by measuring non-irradiated parts and selecting the ones with the best performance. However, the data in the present work show that performance at high doses is not correlated to the pre-irradiation performance. Thus, this method is not effective. Instead, a predictive method based on a combination of device parameters may be more practical, as suggested above.

When tight statistical bounds are required at high dose for a component, it may become impossible to use pre-existing, off-the-shelf components. Instead, a more practical approach is to design custom, application-specific integrated circuits such that their post-

irradiation tolerances are still within specifications. Such an approach requires statistical characterization, as done in the present work, combined with modeling of devices to include TID response, such as in [42]. MC tools native to integrated circuit design tools (e.g., Cadence Virtuoso [67]) can then be leveraged in design.

For SiGe HBTs, and for bipolar transistors in general, Equation 2.5 and Equation 2.7 are meaningful in design for radiation-rich environments at both the process and circuit levels. From a device perspective, reducing process variation, especially in the base, will naturally improve the variability and predictability of TID response. For circuits, biasing at higher V_{BE} will prevent the increase of both $\mu[I_B]$ and $\sigma[I_B]$, mitigating performance degradation at the cost of power consumption. When considering statistical yield as well, a new dimension is added to design, where post-irradiation variability versus performance is a trade-off that should be considered.

2.6 Summary

Characterization of a 40 SiGe HBTs for TID response revealed trends of increasing standard deviation and decreasing pre-to-post-irradiation correlation with increasing dose. Inverse-mode operation was not found to prevent this behavior. These statistical trends were traced to the pre-existing process variation between devices. A simulation methodology was demonstrated in TCAD, which confirmed that process variation can cause increased variability and decreased pre-to-post-irradiation correlation. Further, the mechanism causing the decreased correlation was traced to the trade of dominance between emitter profile for drift-diffusion current and base profile for G/R current. The results highlight the need to perform statistical testing for components meant for high-dose applications and reveal a new dimension of design post-irradiation variability needs to be considered.

CHAPTER 3

DESIGN OF A KA-BAND VG-LNA FOR SPACE APPLICATIONS

3.1 Circuit Design

3.1.1 Gain Control

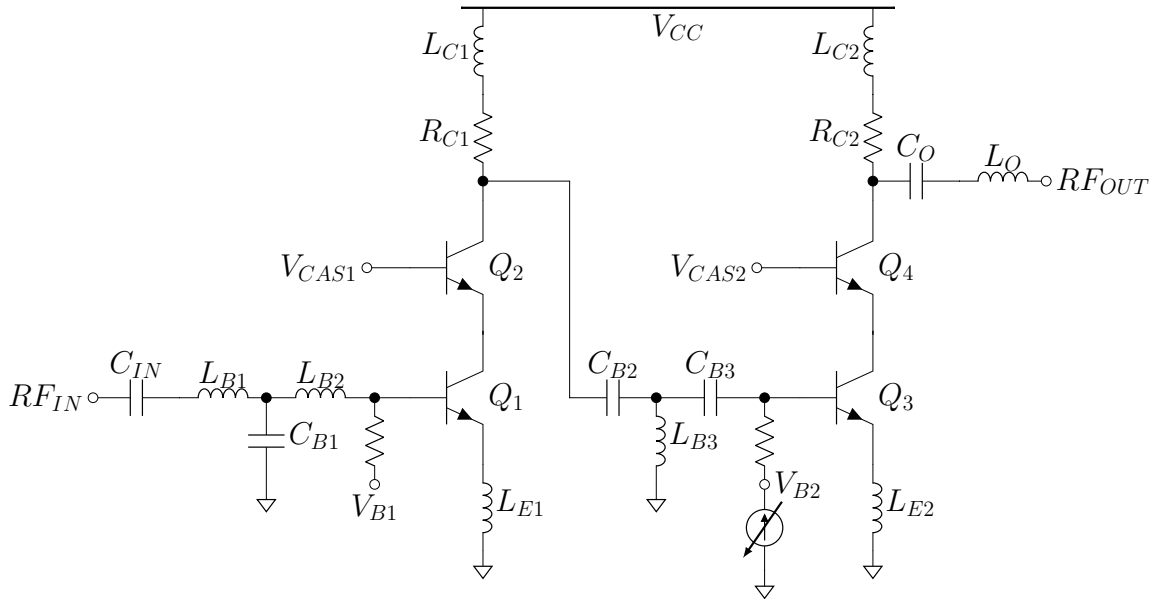


Figure 3.1: Schematic of the designed amplifier.

Table 3.1: VG-LNA Component Values

Q_1	$0.1 \times 4 \times 3$	Q_2	$0.1 \times 4 \times 3$		
Q_3	$0.1 \times 8 \times 3$	Q_4	$0.1 \times 8 \times 3$		
L_{B1}	110 pH	C_{B1}	78 fF	L_{B2}	340 pH
L_{E1}	60 pH	R_{C1}	5 Ω	L_{C1}	370 pH
C_{B2}	19 fF	L_{B3}	200 pH	C_{B3}	58 fF
L_{E2}	50 pH	R_{C2}	7 Ω	L_{C2}	280 pH
C_{IN}	0.8 pF	C_O	0.5 pF	L_O	150 pH

Device sizes are given as width (μm) \times length (μm) \times number of devices.

A popular technique for implementing variable gain is current stealing [68, 69, 70], in which a shunting RF path is switched on and off to “steal” signal from the amplifier output.

While effective, current stealing simply discards available signal, which is inefficient. In the present work, a bias tuning approach is selected instead, which saves power when only low gain is needed, improving system efficiency. A common problem with bias-tuned variable-gain amplifiers (VGAs) is the nonlinear bias-to-gain translation. To overcome this limitation, the present work integrates a linear-in-dB control circuit in the form of a current-steering DAC. The co-integrated design alleviates the need for extensive external gain calibration.

The present work demonstrates the design, implementation, and characterization of a SiGe VG-LNA for emerging K_a -band radar and communications applications. The measured VG-LNA exhibits state-of-the-art performance for both noise figure and DC power consumption across wide bandwidth and gain-tuning range.

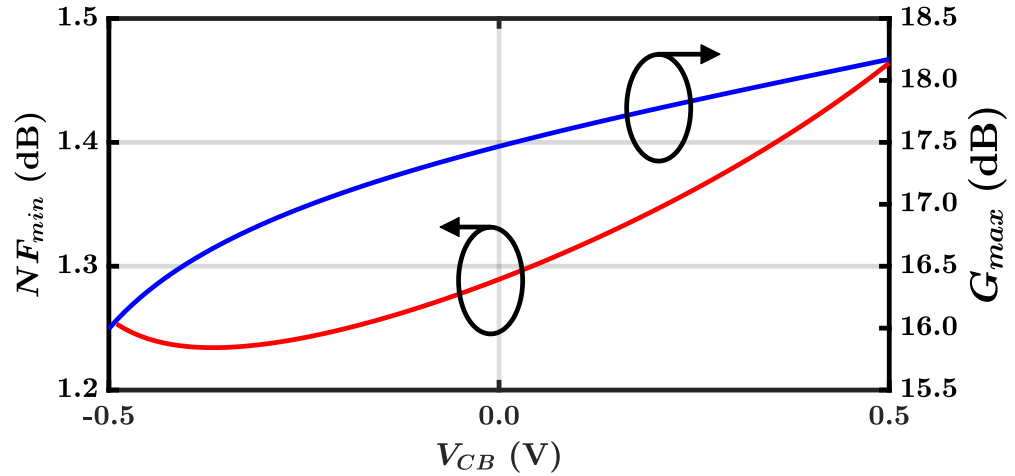


Figure 3.2: Simulated minimum noise figure and maximum available gain for the first stage as a function of V_{CB} of Q_1 .

3.1.2 Low-Noise Amplifier

The VG-LNA was implemented in GF BiCMOS9HP, the same process technology as in chapter 2. It has previously been shown that this SiGe technology platform is robust to total ionizing radiation and single-event latch-up, making it ideal for orbital space applications [3]. EMX was used for electromagnetic simulation [71].

The schematic of the designed SiGe VG-LNA is shown in Figure 3.1. Corresponding component values are listed in Table 3.1. A two-stage cascode amplifier topology is used. To optimize both noise and power consumption (P_{DC}), fixed bias V_{B1} sets stage one at minimum NF_{min} . This relatively low bias still provides sufficient gain to suppress the noise of stage two. Then, bias tuning is applied at V_{B2} to achieve variable gain in stage two. The resonant loads of either stage are tuned to give gain flatness across the desired band.

To optimize for both noise and DC power, P_{DC} , V_{CAS1} and V_{CAS2} are set to 1.6 V, pushing Q_1 and Q_3 into weak saturation. Then, the supply voltage can also be lowered to 1.6 V. Q_2 and Q_4 thus remain in forward-active mode, preventing further degradation in maximum available gain, G_{max} due to their CB-junction capacitances. Previous work has shown that SiGe HBTs in weak saturation still provide substantial RF performance [72, 73]. Beyond saving power, $V_{CB} < 0$ also slightly reduces NF_{min} , though available gain is also reduced. Simulations of this trade-off are shown in Figure 3.2. For this design, a 1.6 V supply set V_{CB} at -0.2 V, giving 10–20% power savings over a more typical 2 V supply at an acceptable 2 dB degradation in G_{max} .

Inductive degeneration, L_{E1} and L_{E2} , allow simultaneous noise and gain matching both at the input and between stages. V_{B1} is relatively low, making broadband input matching more difficult. To compensate, a two-section input-matching network is used. Due to the high-quality RF metals and physical separation from the lossy silicon substrate in the 9HP platform, the extra inductor, L_{B1} , has little insertion loss ($Q \approx 30$), contributing negligible degradation in noise figure.

3.1.3 Digital-to-Analog Converter

An on-chip current-steering DAC was designed to facilitate bias tuning. The schematic is shown in Figure 3.3. An external bias current of 10 μA is applied to the input NPN, Q_{DAC0} . Q_{DAC1} - Q_{DAC16} are individually sized to achieve gain steps of 1 dB, a benefit

of co-designing the amplifier and DAC. T_1 - T_{16} are used as analog switches to steer the currents of Q_{DAC1} - Q_{DAC16} , which are summed at the output pMOS mirror, T_0 and T_{OUT} . Finally, Q_B performs I-to-V conversion to generate V_{B2} . Because the bias steps required to attain linear-in-dB steps of gain are not constant, a non-uniform thermometer coding scheme was utilized. A binary-to-thermometer decoder was also implemented on-chip. These integrated control circuits simplify the system-level control complexity.

Figure 3.3: Schematic of the integrated DAC.

A micrograph of the designed VG-LNA is shown in Figure 3.4. In measurement, a Keysight E36300 power supply was used to generate supply voltages. Keithley 2400 Source Meters were used to drive V_{B1} and the $10\ \mu\text{A}$ DAC reference current. The supply voltages were 1.6 V for the LNA, 2.2 V for the DAC, and 1.2 V for the digital logic. The input stage of the LNA was fixed at 7 mA quiescent current. A plot of DC power consumption over the various gain states is shown in Figure 3.5. Power consumption ranges from 12.0–17.3 mW over gain states for the LNA alone, or 13.2–21.7 mW including the DAC.

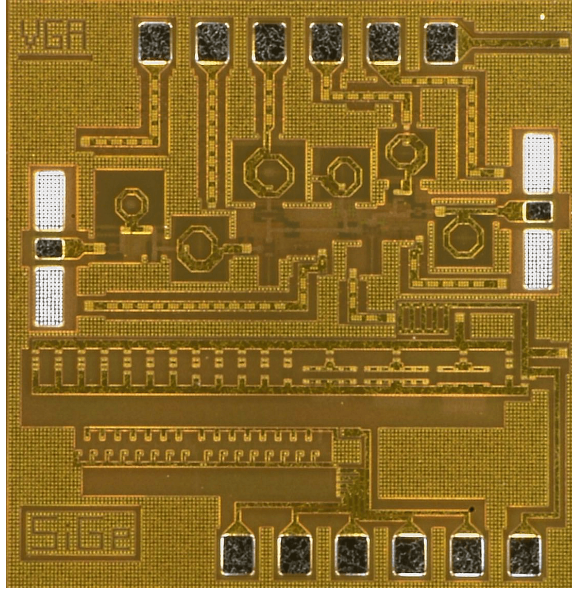


Figure 3.4: Die micrograph of fabricated VG-LNA. The total area, including DC and RF pads, is $1.50 \times 1.54 \text{ mm}^2$. The area of the LNA without the DAC is $1.35 \times 0.44 \text{ mm}^2$.

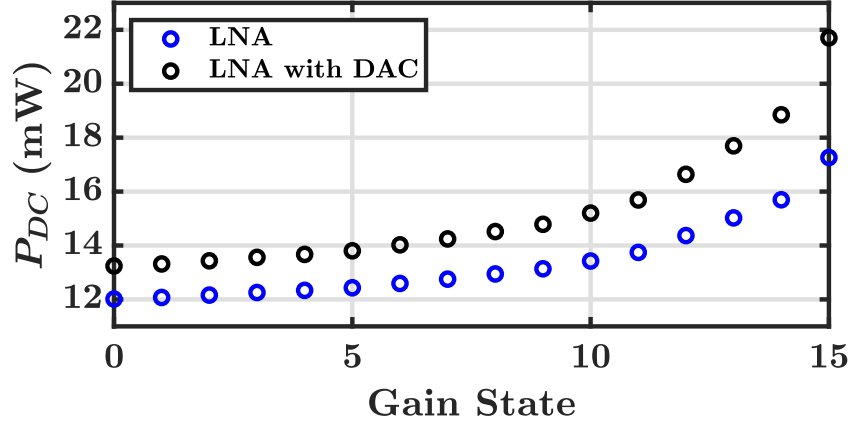
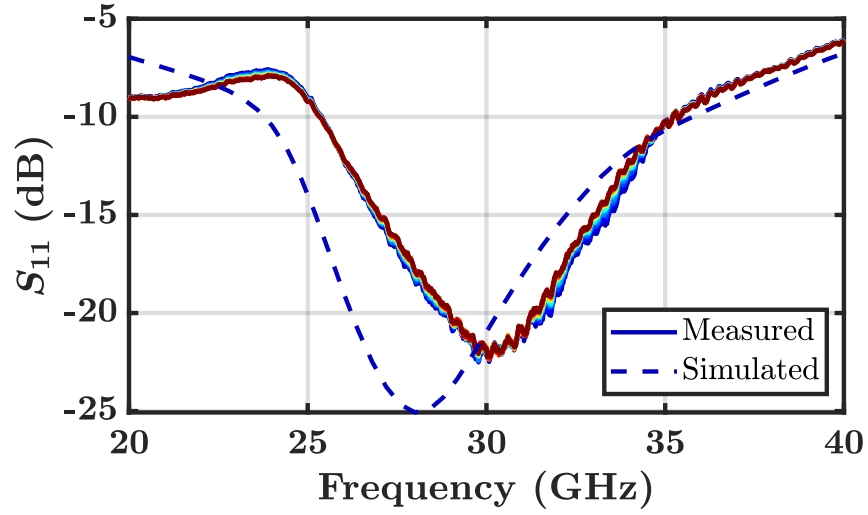


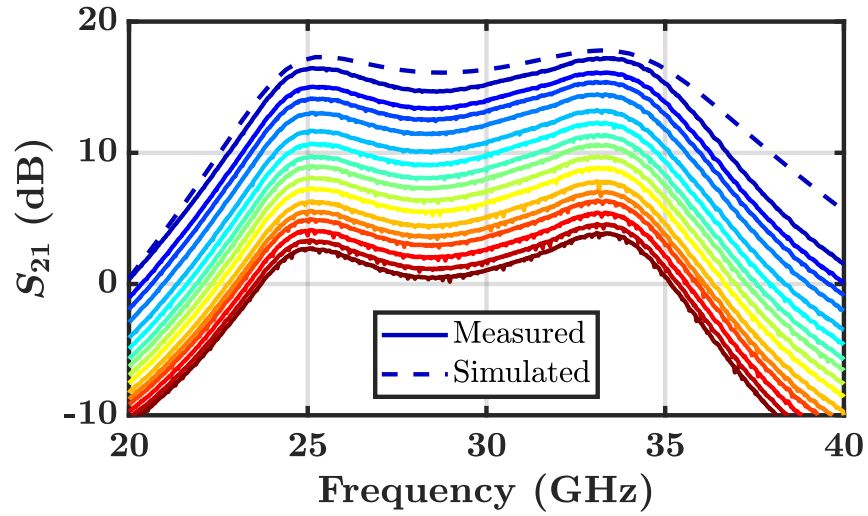
Figure 3.5: DC power consumption over gain states showing variation from 12.0–17.3 mW for the LNA alone or 13.2–21.7 mW including the DAC.

work analyzer via on-die probing with RF and DC probes from GGB Industries Inc. Open and short structures were used to de-embed the effects of the RF pads [74]. The measured input matching and small-signal gain across frequency for all 16 gain states are shown in Figure 3.6a and Figure 3.6b, respectively. Input matching is independent of gain state, since the input stage has fixed bias and the cascode configuration provides excellent reverse isolation. The results demonstrate nearly constant bandwidth from 26–35 GHz, limited by

−10 dB input matching.



(a)



(b)

Figure 3.6: Plots of (a) input matching and (b) small-signal gain across frequency for all 16 gain states. Both gain and matching bandwidth are maintained for all gain states. The dashed lines show the simulated result for the highest gain state.

The peak gain for each state is shown in Figure 3.7a, varying from 4.0 to 18.5 dB, occurring at 33.5 GHz for all gain states. The corresponding gain steps are shown in Figure 3.7b, highlighting nearly linear-in-dB steps.

RMS phase error ($\Delta\phi$), averaged over all gain states, is shown in Figure 3.8. The error

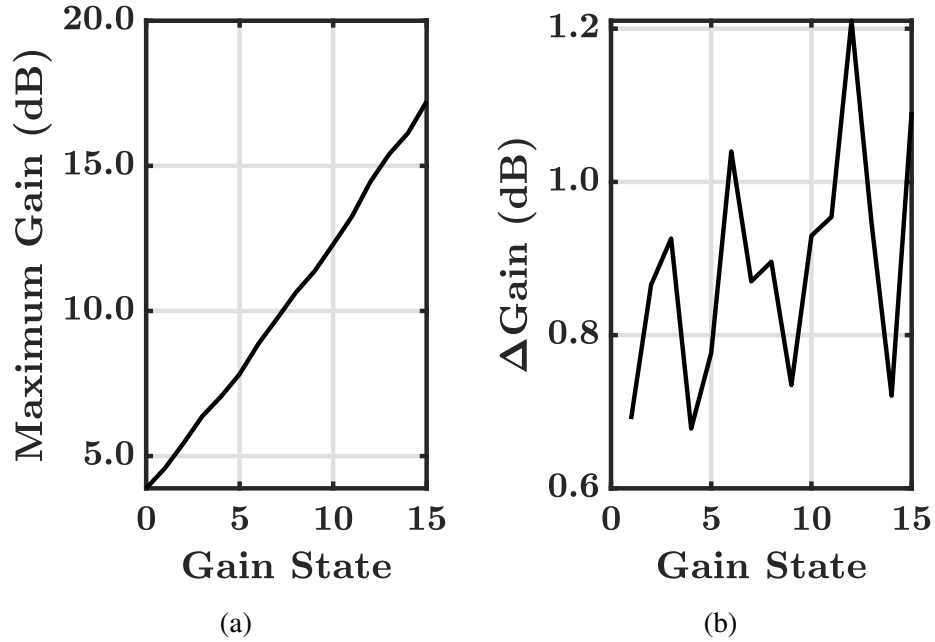


Figure 3.7: (a) Gain over tune state and (b) corresponding change in gain over tune state.

remains less than 6° until 32 GHz, peaking to 10° at 35 GHz. The phase error peak is a result of the bias-tuned topology. Changing the bias current of the second stage also varies the base-emitter capacitance of Q_3 , causing the insertion phase to change with state. In design, the height of the phase-error peak can be reduced by biasing the second stage at higher quiescent currents, and comes at a trade-off of power and gain-bandwidth. In this work, higher phase error was accepted in order to reduce power consumption. The result still demonstrates very competitive phase error from 26–32 GHz.

An Agilent N9030A PXA signal analyzer and Agilent 346C noise source were used to characterize noise figure. Cable losses and impedance mismatches were calibrated out. The measured NF is shown in Figure 3.9 as a function of frequency for the highest gain state. A minimum NF of 3 dB is achieved at 26 GHz, the lowest reported value among comparable amplifiers. This low noise figure highlights the efficacy of the VG-LNA approach. Since a DSA is no longer required, this approach promises even greater noise savings at the receiver level.

Large-signal linearity was measured using an Agilent E8257D PSG analog signal gen-

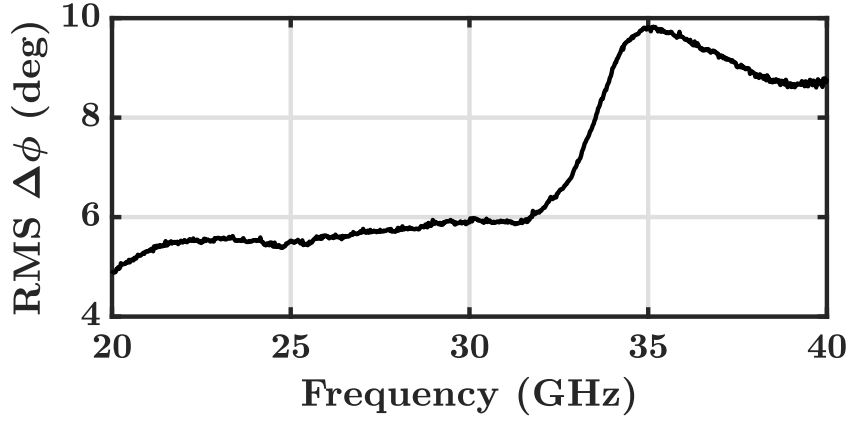


Figure 3.8: RMS phase error, $\Delta\phi$, across frequency with a peak of 10° near 35 GHz.

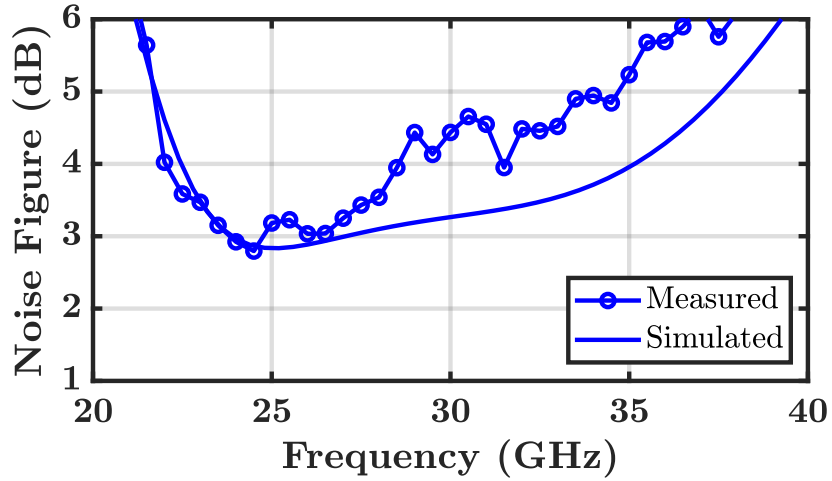


Figure 3.9: NF across frequency for the highest gain state, < 5 dB across the bandwidth. Circles indicate measured frequencies.

erator and Agilent N9030A PXA signal analyzer. Figure 3.10 shows large-signal power sweeps taken at 26 GHz for selected gain states. The extracted input 1-dB compression point (IP_{1dB}) is shown to be -24 dBm. Over frequency and gain state, IP_{1dB} was found to vary between -29 and -22 dBm.

3.2.1 Performance Comparison

Table 3.2 compares silicon-based VG-LNAs at similar operating frequencies. The demonstrated design offers the lowest noise figure and the widest gain tuning range except for [75], which uses a DSA. Phase error remains below a very competitive 6° until 32 GHz, while

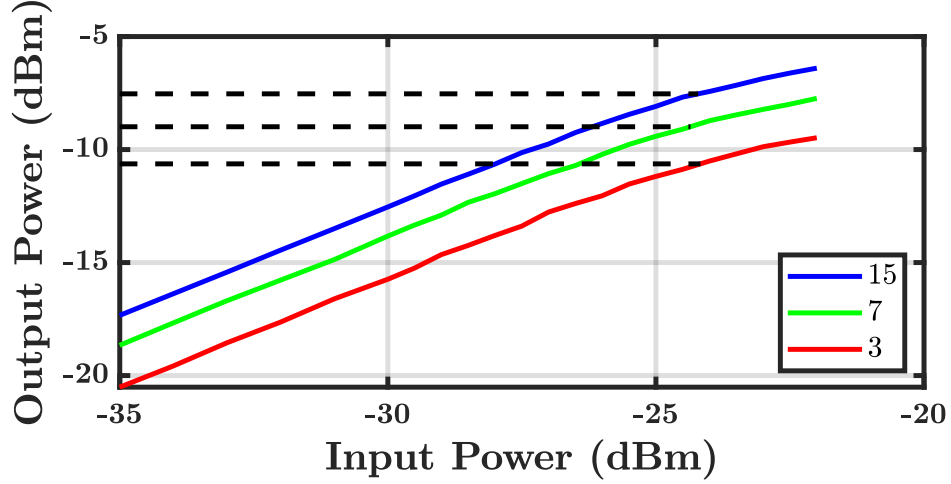


Figure 3.10: Large-signal power sweeps for selected gain states at 26 GHz with dashed lines showing extraction of IP_{1dB} of -24 dBm.

peak phase error reaches 10° at the upper band edge. For full-band operation the slight trade-off in phase error to reduce noise and power remains attractive for power-constrained applications such as space systems. When compared to [76], the present design offers 3.5 dB higher gain range and lower DC power. Furthermore, this work is the only analog-based tuning method that uses an integrated DAC with co-designed bias steps.

The present work highlights the receiver performance that can be achieved when combining an LNA and DSA into a unified VG-LNA topology. Whereas current stealing approaches waste power by shunting it away, the present work uses bias tuning, which enhances receiver efficiency. Optimization of noise and power was performed using weakly saturated SiGe HBTs. For space applications from 26–32 GHz the resulting amplifier demonstrates state-of-the-art noise figure and power consumption with the widest tuning range among non-attenuator designs and less than 6° phase error, and is the only analog-tunable design with integrated bias control. The presented VG-LNA is well-suited for emerging, power-constrained, radar and communications applications such as CubeSat and SmallSat constellations.

Table 3.2: Comparison of State-of-the-Art, Silicon-Based, Variable-Gain LNAs

Ref.	Tech.	Gain Tune Topology	BW (GHz)	Gain Range (dB)	NF (dB)	IP_{1dB} (dBm)	$\Delta\phi$ (deg)	P_{DC} (mW)	Area (mm ²)	Integrated Control
[77]	180 nm CMOS	Bias Tune	26.6	-5.4 – 8.8	8.3	-16	8.9	25.7	0.65	None
[78]	65-nm CMOS	Bias Tune	30 – 34.5	10.2 – 20.8	3.71 ⁽¹⁾	-20.4 ⁽¹⁾	8	16.5 – 26.7	0.2	None
[79]	90-nm CMOS	Curr. Steal.	34.7 – 39.2	18.9/16.5/8.4	6.74 ⁽¹⁾	-20/-15/-7	—	15.62	0.203	None
[76]	120-nm SiGe	Curr. Steal.	26 – 40	9 – 20	3.4 – 4.3	-27	2.5	33	0.13	Binary
[75]	65-nm CMOS	DSA	33.5 – 39	-10 – 21	4 ⁽¹⁾	-22 ⁽¹⁾	5.4	28	1.05	Binary
[80] ⁽³⁾	40-nm CMOS	Curr. Steal.	27 – 33	-6.5 – 1	6.62 ⁽¹⁾	2.5 ⁽¹⁾	—	11.85	0.08	Binary
This Work	90-nm SiGe	Bias Tune	26 – 32	4 – 18.5	3 – 5	-29 – -22	6	13.2 – 21.7	0.59	On-chip DAC
			26 – 35				10			

1 = Not characterized over gain state, 2 = With integrated DAC, 3 = Simulation only

CHAPTER 4

IMPACT OF VARIABILITY ON CIRCUIT PERFORMANCE

4.1 Current Mirrors

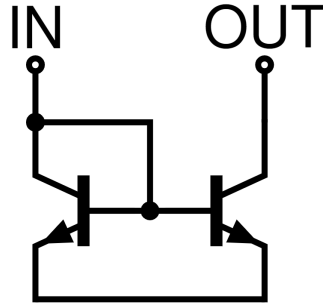


Figure 4.1: Schematic of a simple CM.

Consider a simple CM composed of two nominally identical transistors, the schematic of which is shown in Figure 4.1. The mirror ratio of this CM is less than unity because of both the Early effect and the finite current gain, β , of the transistors. Assuming a proper design, the Early effect should not be a strong factor, so the main cause of random mismatches can be attributed to variations in β .

Observing the data in Figure 2.3, the increase in I_B is equivalent to a decrease in β . As an example, the mean peak β decreases from 450 to 150 at the maximum TID with the standard deviation increasing from 30 to 50. These parameters are used to perform a MC analysis on the mirror ratio of the CM.

In MATLAB, 10,000 random pairs of (β_1, β_2) were from Gaussian distributions with means and standard deviations taken from the TID data. These pairs of β were used to evaluate the theoretical mirror ratio of the simple CM in Equation 4.1, A_I .

$$A_I = \frac{1}{1 + \frac{1}{\beta_1} + \frac{1}{\beta_2}} \quad (4.1)$$

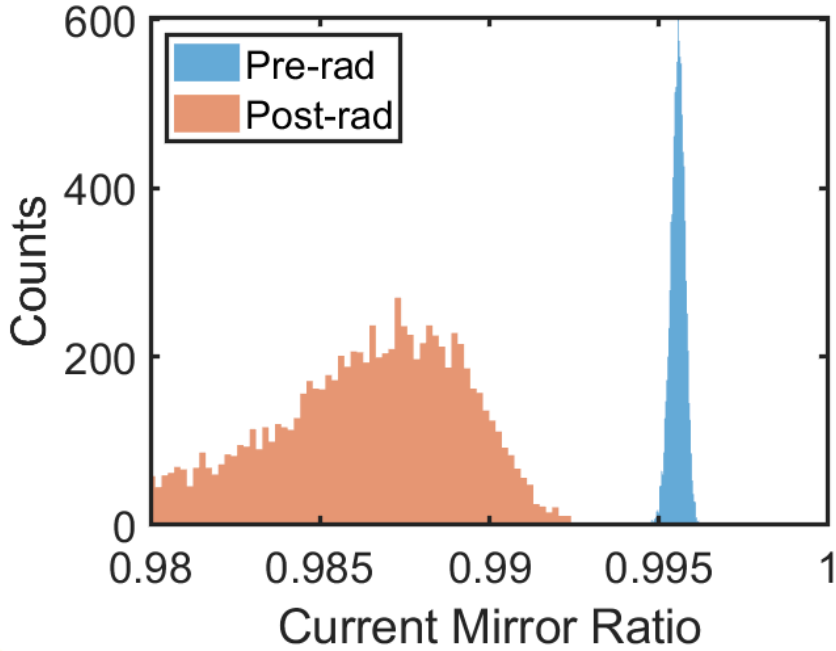


Figure 4.2: MC simulations of the mirror ratio of a current mirror before and after irradiation.

The results are shown in Figure 4.2. Due to the decrease in mean β , the average A_I also decreases. However, the simultaneous increase in standard deviation also causes the histogram of A_I to spread out drastically at 2 Mrad(SiO₂).

4.2 Current-Steering Digital-to-Analog Converter

The data for the CMs above readily translates to the behavior of current-steering DACs, the same topology as in the presented VG-LNA. To demonstrate a possible worst case, a purely binary encoding was selected. The DAC is assumed to be composed of nominally identical unit cells. Each bit b in the weighting is created by a summation of 2^b unit cells, and the DAC is set to have $B = 4$ bits, similar to that in the VG-LNA. To perform the Monte Carlo simulation, the current of each of the binary cells is

$$I_b = I_0 A_I 2^b \quad (4.2)$$

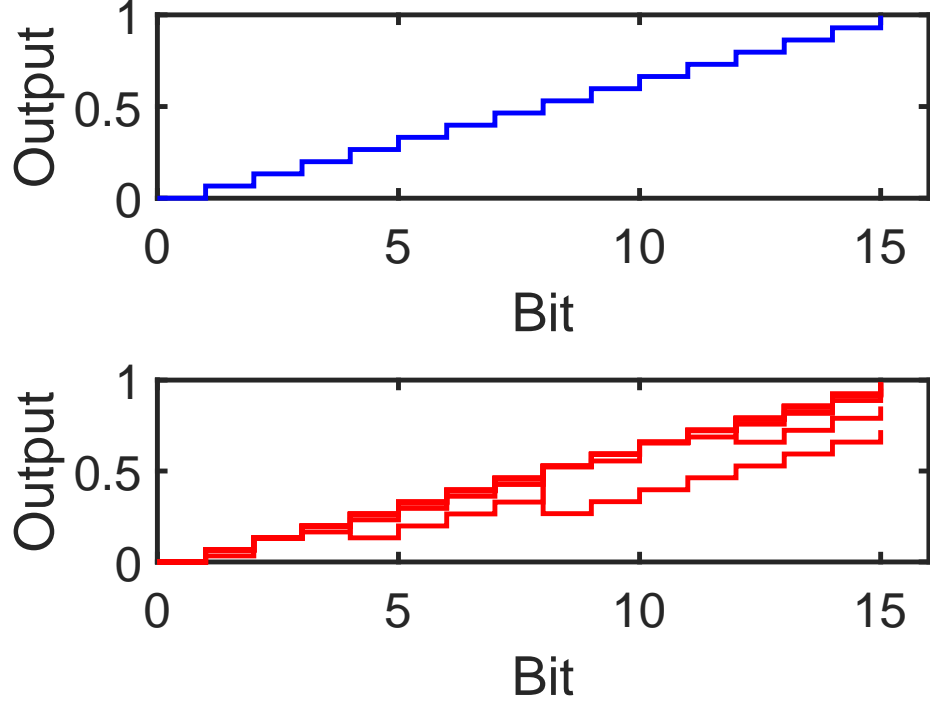


Figure 4.3: MC simulations DAC transfer curves before (above) and after (below) irradiation.

where I_0 is some reference current, A_I is the current gain in Equation 4.1, and b is the bit number. The I_b are summed according to the selected binary state. For each Monte Carlo point, the β of every transistor in the circuit was randomized.

First, the DAC transfer curve is shown in Figure 4.3. Due to the decreased β of the constituent transistors, the gain error decreases on the average, which is not necessarily a concern if proper DAC calibration is available. However, the increase in the standard deviation of β also leads to impacted linearity. In some cases, if the mismatch is severe on the most significant bit of the DAC, the transfer characteristic can become non-monotonic.

The simulated results for the DNL and INL are shown in Figure 4.4 and Figure 4.5, respectively. The worst-case DNL increases from 0.002 least-significant bits (LSBs) before irradiation to almost 3 LSB after 2 Mrad(SiO_2). The worst-case post-irradiation INL was as large as 5 LSB. From these results, it is clear that, even though the SiGe HBT is considered TID-tolerant for RF applications, their use in DACs can still be strongly impacted by TID due to exasperated variability amongst devices.

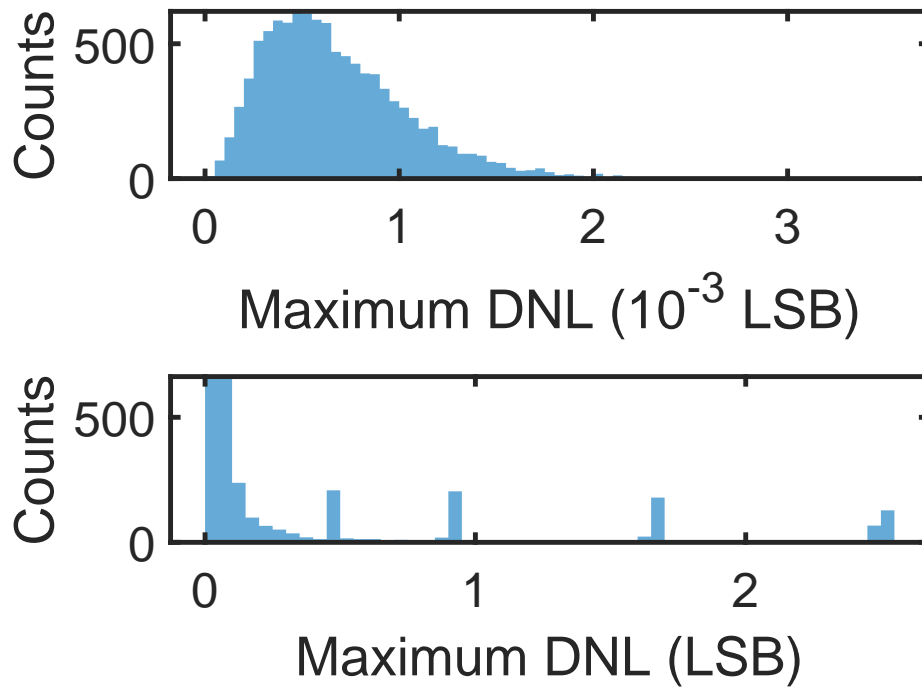


Figure 4.4: MC simulations DAC DNL before (above) and after (below) irradiation.

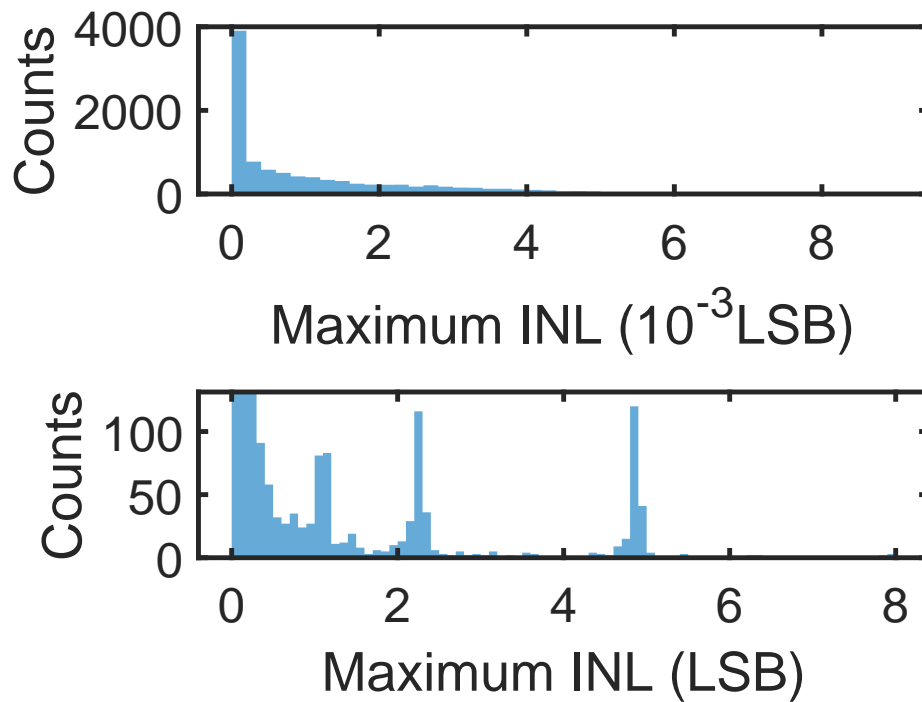


Figure 4.5: MC simulations DAC INL before (above) and after (below) irradiation.

CHAPTER 5

FUTURE WORK

Thus far, the impact of the variability in TID response has been shown using analytical theory and MC simulation. In order to properly evaluate the system-level complications that may arise, characterization must be performed. Possible circuits of interest are

- **Current Mirrors:** Current mirrors are a key building block in analog circuits like bias blocks and data converters. Different topologies of current mirrors such as cascode current mirrors can be studied to find optimal conditions for current mirror performance subject to TID.
- **Data Converters:** Data converter linearity and noise performance can be limited by device-to-device performance matching. This was shown for binary-weighted current-steering DACs in chapter 4. Further theoretical examination and characterization are warranted to compare coding schemes and device layout techniques to mitigate TID-induced variability.
- **Frequency Converters:** Mixers, frequency multipliers, and oscillators are all susceptible to performance degradation due to device mismatch. Possible weaknesses are worsened harmonic suppression and increased common-mode noise. Given the complex nature of these circuits, TID characterization of test circuits will be required to examine these degradations.

CHAPTER 6

CONCLUSION

An exaggeration of mismatch following exposure to TID was observed for 90-nm SiGe HBTs, which was tied to preexisting process variations in the base and emitter dopings. This increasing mismatch was shown to be a potential concern for DACs. Since DACs are common components in RF receiver systems, for instance to implement tunable performance in a VG-LNA, degradation in linearity due to increased mismatch can impair these systems. Further investigation is necessary to understand the full system-level implications and failure mechanisms that can arise from device-to-device mismatch in TID-sensitive applications such as science missions to Europa.

Appendices

APPENDIX A

DERIVATION OF BASE CURRENT CORRELATION

The definition of the correlation coefficient between random variables X and Y was given in Equation 2.6. Letting X be the pre-irradiation base current, I_{B0} , and Y be the post-irradiation base current, $I_{B0} + \Delta I_B$, the pre-to-post correlation can be derived from the standard rules of covariance as follows:

$$\rho[\text{pre, post}] = \frac{C[I_{B0} + \Delta I_B, I_{B0}]}{\sigma[I_{B0}]\sigma[I_{B0} + \Delta I_B]} \quad (\text{A.1})$$

$$= \frac{C[I_{B0}, I_{B0}] + C[I_{B0}, \Delta I_B]}{\sigma[I_{B0}]\sigma[I_{B0} + \Delta I_B]} \quad (\text{A.2})$$

$$= \frac{\text{Var}[I_{B0}] + C[I_{B0}, \Delta I_B]}{\sigma[I_{B0}]\sigma[I_{B0} + \Delta I_B]} \quad (\text{A.3})$$

where the covariance between I_{B0} and ΔI_B can be expanded as

$$C[I_{B0}, \Delta I_B] = N_{it}C[g, h]e^{3qV_{BE}/2kT} \quad (\text{A.4})$$

Substituting in the previously derived expressions for I_{B0} and ΔI_B in Equation 2.8 and Equation 2.9, respectively, and the variance in Equation 2.5, again assuming $C[g, h]$ is negligible,

$$\rho[\text{pre, post}] \approx \frac{\text{Var}[g]e^{2qV_{BE}/kT}}{\sigma[g]e^{qV_{BE}/kT}\sqrt{g^2e^{2qV_{BE}/kT} + N_{it}^2h^2e^{qV_{BE}/kT}}} \quad (\text{A.5})$$

$$= \frac{\sigma[g]}{\sqrt{\text{Var}[g] + N_{it}^2\text{Var}[h]e^{-qV_{BE}/kT}}} \quad (\text{A.6})$$

REFERENCES

- [1] J. Babcock, J. Cressler, L. Vempati, S. Clark, R. Jaeger, and D. Hareme, "Ionizing radiation tolerance and low-frequency noise degradation in UHV/CVD SiGe HBT's," *IEEE Electron Device Letters*, vol. 16, no. 8, pp. 351–353, Aug. 1995.
- [2] R. Reed, P. Marshall, H. Ainspan, C. Marshall, H. Kim, J. Cressler, G. Niu, and K. LaBel, "Single event upset test results on a prescaler fabricated in IBM's 5HP silicon germanium heterojunction bipolar transistors BiCMOS technology," in *2001 IEEE Radiation Effects Data Workshop. NSREC 2001. Workshop Record.*, IEEE.
- [3] J. D. Cressler, "Radiation effects in SiGe technology," *IEEE Transactions on Nuclear Science*, vol. 60, no. 3, pp. 1992–2014, Jun. 2013.
- [4] J. Metcalfe, D. E. Dorfan, A. A. Grillo, A. Jones, D. Lucia, F. Martinez-McKinney, M. Mendoza, M. Rogers, H. F.-W. Sadrozinski, A. Seiden, E. Spencer, M. Wilder, J. D. Cressler, G. Prakash, and A. Sutton, "Evaluation of the radiation tolerance of SiGe heterojunction bipolar transistors under 24-GeV proton exposure," *IEEE Transactions on Nuclear Science*, vol. 53, no. 6, pp. 3889–3893, Dec. 2006.
- [5] E. O. Mikkola and J. D. Cressler, "12-bit, 3GS/s, radiation-hard time-interleaved adc for particle accelerator applications," in *2012 IEEE Nuclear Science Symposium and Medical Imaging Conference Record (NSS/MIC)*, IEEE, Oct. 2012.
- [6] Z. E. Fleetwood, E. W. Kenyon, N. E. Lourenco, S. Jain, E. X. Zhang, T. D. England, J. D. Cressler, R. D. Schrimpf, and D. M. Fleetwood, "Advanced SiGe BiCMOS technology for multi-Mrad electronic systems," *IEEE Transactions on Device and Materials Reliability*, vol. 14, no. 3, pp. 844–848, Sep. 2014.
- [7] P. S. Chakraborty, A. S. Cardoso, B. R. Wier, A. P. Omprakash, J. D. Cressler, M. Kaynak, and B. Tillack, "A 0.8 THz f_{\max} SiGe HBT operating at 4.3 K," *IEEE Electron Device Letters*, vol. 35, no. 2, pp. 151–153, Feb. 2014.
- [8] D. Manger, W. Liebl, S. Boguth, B. Binder, K. Aufinger, C. Dahl, C. Hengst, A. Pribil, J. Oestreich, S. Rohmfeld, S. Rothenhaeusser, D. Tschumakow, and J. Boeck, "Integration of SiGe HBT with $f_T = 305$ GHz, $f_{\max} = 537$ GHz in 130nm and 90nm CMOS," in *2018 IEEE BiCMOS and Compound Semiconductor Integrated Circuits and Technology Symposium (BCICTS)*, IEEE, Oct. 2018.
- [9] V. P. Trivedi, J. P. John, J. Young, T. Dao, D. Morgan, I. To, R. Ma, D. Hammock, S. Mehrotra, L. Radic, B. Grote, T. Roggenbauer, and J. Kirchgessner, "A 90nm BiCMOS technology featuring 400GHz f_{\max} SiGe:C HBT," in *2016 IEEE Bipolar/BiCMOS Circuits and Technology Meeting (BCTM)*, IEEE, Sep. 2016.

- [10] L. Pantoli, H. Bello, G. Leuzzi, H. J. Ng, and D. Kissinger, “SiGe sub-THz VCOs design approach for imaging applications,” in *2020 International Workshop on Integrated Nonlinear Microwave and Millimetre-Wave Circuits (INMMiC)*, IEEE, Jul. 2020.
- [11] J. R. Schwank, M. R. Shaneyfelt, D. M. Fleetwood, J. A. Felix, P. E. Dodd, P. Paillet, and V. Ferlet-Cavrois, “Radiation effects in MOS oxides,” *IEEE Transactions on Nuclear Science*, vol. 55, no. 4, pp. 1833–1853, Aug. 2008.
- [12] N. E. Lourenco, R. L. Schmid, K. A. Moen, S. D. Phillips, T. D. England, J. D. Cressler, J. Pekarik, J. Adkisson, R. Camillo-Castillo, P. Cheng, J. E. Monaghan, P. Gray, D. Hame, M. Khater, Q. Liu, A. Vallett, B. Zetterlund, V. Jain, and V. Kaushal, “Total dose and transient response of SiGe HBTs from a new 4th-generation, 90 nm SiGe BiCMOS technology,” in *2012 IEEE Radiation Effects Data Workshop*, IEEE, Jul. 2012.
- [13] B. Mossawir, I. R. Linscott, U. S. Inan, J. L. Roeder, J. V. Osborn, S. C. Witczak, E. E. King, and S. D. LaLumondiere, “A TID and SEE radiation-hardened, wide-band, low-noise amplifier,” *IEEE Transactions on Nuclear Science*, vol. 53, no. 6, pp. 3439–3448, Dec. 2006.
- [14] D. C. Howard, A. S. Cardoso, Z. E. Fleetwood, N. E. Lourenco, T. D. England, P. K. Saha, S. Shankar, R. M. Diestelhorst, E. X. Zhang, C. X. Zhang, P. Paki-Amouzou, and J. D. Cressler, “Mitigation of total dose performance degradation in an 8–18 GHz SiGe reconfigurable receiver,” *IEEE Transactions on Nuclear Science*, vol. 61, no. 6, pp. 3226–3235, Dec. 2014.
- [15] H. Ohyama, J. Vanhellemont, Y. Takami, K. Hayama, H. Sunaga, J. Poortmans, and M. Caymax, “Degradation of $\text{Si}_{1-x}\text{Ge}_x$ epitaxial heterojunction bipolar transistors by 1-MeV fast neutrons,” *IEEE Transactions on Nuclear Science*, vol. 42, no. 6, pp. 1550–1557, 1995.
- [16] D. I. Sotskov, V. V. Elesin, A. G. Kuznetsov, N. M. Zhidkov, I. O. Metelkin, K. M. Amburkin, D. M. Amburkin, N. A. Usachev, D. V. Boychenko, and V. V. Elesina, “Displacement damage effects mitigation approach for heterojunction bipolar transistor frequency synthesizers,” *IEEE Transactions on Nuclear Science*, vol. 67, no. 11, pp. 2396–2404, Nov. 2020.
- [17] J. Roldan, W. Ansley, J. Cressler, S. Clark, and D. Nguyen-Ngoc, “Neutron radiation tolerance of advanced UHV/CVD SiGe HBT BiCMOS technology,” *IEEE Transactions on Nuclear Science*, vol. 44, no. 6, pp. 1965–1973, 1997.
- [18] N. E. Lourenco, S. Zeinolabedinzadeh, A. Ildefonso, Z. E. Fleetwood, C. T. Coen, I. Song, S. Jung, F. Inanlou, N. J.-H. Roche, A. Khachatrian, D. McMorro, S. P. Buchner, J. H. Warner, P. Paki, and J. D. Cressler, “An investigation of single-event

effect modeling techniques for a SiGe RF low-noise amplifier,” *IEEE Transactions on Nuclear Science*, vol. 63, no. 1, pp. 273–280, Feb. 2016.

- [19] A. Ildefonso, N. E. Lourenco, Z. E. Fleetwood, M. T. Wachter, G. N. Tzintzarov, A. S. Cardoso, N. J.-H. Roche, A. Khachatrian, D. McMorrow, S. P. Buchner, J. H. Warner, P. Paki, M. Kaynak, B. Tillack, and J. D. Cressler, “Single-event transient response of comparator pre-amplifiers in a complementary SiGe technology,” *IEEE Transactions on Nuclear Science*, vol. 64, no. 1, pp. 89–96, Jan. 2017.
- [20] S. Zeinolabedinzadeh, H. Ying, Z. E. Fleetwood, N. J.-H. Roche, A. Khachatrian, D. McMorrow, S. P. Buchner, J. H. Warner, P. Paki-Amouzou, and J. D. Cressler, “Single-event effects in high-frequency linear amplifiers: Experiment and analysis,” *IEEE Transactions on Nuclear Science*, vol. 64, no. 1, pp. 125–132, Jan. 2017.
- [21] S. Zeinolabedinzadeh, I. Song, U. S. Raghunathan, N. E. Lourenco, Z. E. Fleetwood, M. A. Oakley, A. S. Cardoso, N. J.-H. Roche, A. Khachatrian, D. McMorrow, S. P. Buchner, J. H. Warner, P. Paki-Amouzou, and J. D. Cressler, “Single-event effects in a W-Band (75-110 GHz) radar down-conversion mixer implemented in 90 nm, 300 GHz SiGe HBT technology,” *IEEE Transactions on Nuclear Science*, vol. 62, no. 6, pp. 2657–2665, Dec. 2015.
- [22] A. Ildefonso, I. Song, Z. E. Fleetwood, N. E. Lourenco, M. T. Wachter, G. N. Tzintzarov, and J. D. Cressler, “Modeling single-event transient propagation in a SiGe BiCMOS direct-conversion receiver,” in *2016 16th European Conference on Radiation and Its Effects on Components and Systems (RADECS)*, IEEE, Sep. 2016.
- [23] S. Zeinolabedinzadeh, A. C. Ulusoy, F. Inanlou, H. Ying, Y. Gong, Z. E. Fleetwood, N. J.-H. Roche, A. Khachatrian, D. McMorrow, S. P. Buchner, J. H. Warner, P. Paki, and J. D. Cressler, “Single-event effects in a millimeter-wave receiver front-end implemented in 90 nm, 300 GHz SiGe HBT technology,” *IEEE Transactions on Nuclear Science*, vol. 64, no. 1, pp. 536–543, Jan. 2017.
- [24] A. Ildefonso, C. T. Coen, Z. E. Fleetwood, G. N. Tzintzarov, M. T. Wachter, A. Khachatrian, D. McMorrow, J. H. Warner, P. Paki, and J. D. Cressler, “Utilizing SiGe HBT power detectors for sensing single-event transients in RF circuits,” *IEEE Transactions on Nuclear Science*, vol. 65, no. 1, pp. 239–248, Jan. 2018.
- [25] S. D. Phillips, T. Thrivikraman, A. Appaswamy, A. K. Sutton, J. D. Cressler, G. Vizkelethy, P. Dodd, and R. A. Reed, “A novel device architecture for SEU mitigation: The inverse-mode cascode SiGe HBT,” *IEEE Transactions on Nuclear Science*, vol. 56, no. 6, pp. 3393–3401, Dec. 2009.
- [26] I. Song, S. Jung, N. E. Lourenco, U. S. Raghunathan, Z. E. Fleetwood, S. Zeinolabedinzadeh, T. B. Gebremariam, F. Inanlou, N. J.-H. Roche, A. Khachatrian, D. McMorrow, S. P. Buchner, J. S. Melinger, J. H. Warner, P. Paki-Amouzou, and J. D.

- Cressler, "Design of radiation-hardened RF low-noise amplifiers using inverse-mode SiGe HBTs," *IEEE Transactions on Nuclear Science*, vol. 61, no. 6, pp. 3218–3225, Dec. 2014.
- [27] I. Song, M.-K. Cho, M. A. Oakley, A. Ildefonso, I. Ju, S. P. Buchner, D. McMorro, P. Paki, and J. D. Cressler, "On the application of inverse-mode SiGe HBTs in RF receivers for the mitigation of single-event transients," *IEEE Transactions on Nuclear Science*, vol. 64, no. 5, pp. 1142–1150, May 2017.
 - [28] A. Ildefonso, G. N. Tzintzarov, N. E. Lourenco, Z. E. Fleetwood, A. Khachatrian, S. P. Buchner, D. McMorro, J. H. Warner, M. Kaynak, and J. D. Cressler, "Trade-offs between RF performance and SET robustness in low-noise amplifiers in a complementary SiGe BiCMOS platform," *IEEE Transactions on Nuclear Science*, vol. 67, no. 7, pp. 1521–1529, Jul. 2020.
 - [29] M. Ludwig, E. Daganzo-Eusebio, and M. Davidson, "Ka-band radar missions for Earth observation," in *2013 IEEE Int. Geosci. and Remote Sens. Symp. (IGARSS)*, IEEE, Jul. 2013.
 - [30] D.-W. Kang, J.-G. Kim, B.-W. Min, and G. Rebeiz, "Single and four-element *ka*-band transmit/receive phased-array silicon RFICs with 5-bit amplitude and phase control," *IEEE Transactions on Microwave Theory and Techniques*, vol. 57, no. 12, pp. 3534–3543, Dec. 2009.
 - [31] J. Han, J. Kim, J. Park, and J. Kim, "A ka-band 4-ch bi-directional CMOS t/r chipset for 5g beamforming system," in *2017 IEEE Radio Frequency Integrated Circuits Symposium (RFIC)*, IEEE, Jun. 2017.
 - [32] C.-Y. Chu, Y.-P. Chen, J.-Z. Gao, C.-Y. Ke, Y.-W. Chen, L.-H. Chang, B. Su, T.-S. Chu, and Y.-J. Wang, "A Ka-band scalable hybrid phased array based on four-element ICs," *IEEE Transactions on Microwave Theory and Techniques*, pp. 1–13, 2019.
 - [33] K. K. W. Low, A. Nafe, S. Zehir, T. Kanar, and G. M. Rebeiz, "A scalable circularly-polarized 256-element Ka-band phased-array SATCOM transmitter with $\pm 60^\circ$ beam scanning and 34.5 dBW EIRP," in *2019 IEEE MTT-S International Microwave Symposium (IMS)*, IEEE, Jun. 2019.
 - [34] B.-W. Min and G. M. Rebeiz, "Ka-band BiCMOS 4-bit phase shifter with integrated LNA for phased array T/R modules," in *2007 IEEE MTT-S International Microwave Symposium (IMS)*, IEEE, Jun. 2007.
 - [35] W.-G. Kim, J. P. Thakur, H.-Y. Yu, S.-S. Choi, and Y.-H. Kim, "Ka-band hybrid phase shifter for analog phase shift range extension using 0.13- μ m CMOS technol-

ogy,” in *2010 IEEE International Symposium on Phased Array Systems and Technology*, IEEE, Oct. 2010.

- [36] N. Mazor, O. Katz, R. Ben-Yishay, D. Liu, A. V. Garcia, and D. Elad, “SiGe based Ka-band reflection type phase shifter for integrated phased array transceivers,” in *2016 IEEE MTT-S International Microwave Symposium (IMS)*, IEEE, May 2016.
- [37] Y. Yuan, S.-X. Mu, and Y.-X. Guo, “6-bit step attenuators for phased-array system with temperature compensation technique,” *IEEE Microwave and Wireless Components Letters*, vol. 28, no. 8, pp. 690–692, Aug. 2018.
- [38] Z. Zhang, N. Li, H. Gao, M. Li, S. Wang, Y.-C. Kuan, X. Yu, and Z. Xu, “A DC-32ghz 7-bit passive attenuator with capacitive compensation bandwidth extension technique in 55 nm CMOS,” in *2020 IEEE/MTT-S International Microwave Symposium (IMS)*, IEEE, Aug. 2020.
- [39] K. Wang, T. Zhou, H. Zhang, and L. Qiu, “A 28–40-GHz digital step attenuator with low amplitude and phase variations,” *IEEE Microwave and Wireless Components Letters*, vol. 31, no. 1, pp. 64–67, Jan. 2021.
- [40] A. Worapishet and A. Demosthenous, “Generalized analysis of random common-mode rejection performance of CMOS current feedback instrumentation amplifiers,” *IEEE Trans. Circuits Syst. I*, vol. 62, no. 9, pp. 2137–2146, Sep. 2015.
- [41] R. J. Baker, *CMOS Circuit Design, Layout, and Simulation*. John Wiley & Sons, Ltd, 2011.
- [42] Y. Li, N. Rezzak, E. X. Zhang, R. D. Schrimpf, D. M. Fleetwood, J. Wang, D. Wang, Y. Wu, and S. Cai, “Including the effects of process-related variability on radiation response in advanced foundry process design kits,” *IEEE Trans. Nucl. Sci.*, vol. 57, no. 6, pp. 3570–3574, Dec. 2010.
- [43] D. Corso, S. Libertino, M. Lisiansky, Y. Roizin, F. Palumbo, F. Principato, C. Pace, P. Finocchiaro, and S. A. Lombardo, “Threshold voltage variability of NROM memories after exposure to ionizing radiation,” *IEEE Trans. Electron Devices*, vol. 59, no. 10, pp. 2597–2602, Oct. 2012.
- [44] M. Bagatin, S. Gerardin, F. Ferrarese, A. Paccagnella, V. Ferlet-Cavrois, A. Costantino, M. Muschitiello, A. Visconti, and P.-X. Wang, “Sample-to-sample variability and bit errors induced by total dose in advanced NAND flash memories,” *IEEE Trans. Nucl. Sci.*, vol. 61, no. 6, pp. 2889–2895, Dec. 2014.
- [45] S. Gerardin, M. Bagatin, D. Cornale, L. Ding, S. Mattiazzo, A. Paccagnella, F. Faccio, and S. Michelis, “Enhancement of transistor-to-transistor variability due to total

- dose effects in 65-nm MOSFETs,” *IEEE Trans. Nucl. Sci.*, vol. 62, no. 6, pp. 2398–2403, Dec. 2015.
- [46] S. Gerardin, M. Bagatin, A. Bertoldo, A. Paccagnella, and V. Ferlet-Cavrois, “Sample-to-sample variability of floating gate errors due to total ionizing dose,” *IEEE Trans. Nucl. Sci.*, vol. 62, no. 6, pp. 2511–2516, Dec. 2015.
 - [47] M. Shaneyfelt, J. Schwank, S. Witczak, D. Fleetwood, R. Pease, P. Winokur, L. Riewe, and G. Hash, “Thermal-stress effects and enhanced low dose rate sensitivity in linear bipolar ICs,” *IEEE Trans. Nucl. Sci.*, vol. 47, no. 6, pp. 2539–2545, Dec. 2000.
 - [48] J. Krieg, T. Turflinger, and R. L. Pease, “Manufacturer variability of enhanced low dose rate sensitivity (ELDRS) in a voltage comparator,” *2001 IEEE Radiat. Effects Data Workshop*, pp. 167–171, 2001.
 - [49] J. Guillermin, N. Sukhaseum, A. Varotsou, A. Privat, P. Garcia, M. Vaille, J. Thomas, N. Chatry, and C. Poivey, “Part-to-part and lot-to-lot variability study of TID effects in bipolar linear devices,” in *16th Eur. Conf. on Radiat. and Its Effects on Compon. and Syst. (RADECS)*, IEEE, Sep. 2016.
 - [50] H. Barnaby, C. Cirba, R. Schrimpf, D. Fleetwood, R. Pease, M. Shaneyfelt, T. Turflinger, J. Krieg, and M. Maher, “Origins of total-dose response variability in linear bipolar microcircuits,” *IEEE Trans. Nucl. Sci.*, vol. 47, no. 6, pp. 2342–2349, Dec. 2000.
 - [51] *Radar in a cubesat (RainCube)*, [ONLINE] Available: <https://www.jpl.nasa.gov/cubesat/missions/raincube.php>.
 - [52] J. J. Pekarik, J. Adkisson, P. Gray, Q. Liu, R. Camillo-Castillo, M. Khater, V. Jain, B. Zetterlund, A. DiVergilio, X. Tian, A. Vallett, J. Ellis-Monaghan, B. J. Gross, P. Cheng, V. Kaushal, Z. He, J. Lukaitis, K. Newton, M. Kerbaugh, N. Cahoon, L. Vera, Y. Zhao, J. R. Long, A. Valdes-Garcia, S. Reynolds, W. Lee, B. Sadhu, and D. Hame, “A 90nm SiGe BiCMOS technology for mm-wave and high-performance analog applications,” in *2014 IEEE Bipolar/BiCMOS Circuits and Technol. Meeting (BCTM)*, IEEE, Sep. 2014.
 - [53] D. M. Fleetwood, “Total ionizing dose effects in MOS and low-dose-rate-sensitive linear-bipolar devices,” *IEEE Trans. Nucl. Sci.*, vol. 60, no. 3, pp. 1706–1730, Jun. 2013.
 - [54] Z. E. Fleetwood, A. S. Cardoso, I. Song, E. Wilcox, N. E. Lourenco, S. D. Phillips, R. Arora, P. Paki-Amouzou, and J. D. Cressler, “Evaluation of enhanced low dose rate sensitivity in fourth-generation SiGe HBTs,” *IEEE Trans. Nucl. Sci.*, vol. 61, no. 6, pp. 2915–2922, Dec. 2014.

- [55] A. P. Omprakash, Z. E. Fleetwood, U. S. Raghunathan, A. Ildefonso, A. S. Cardoso, N. E. Lourenco, J. Babcock, R. Mukhopadhyay, E. X. Zhang, P. J. McMarr, D. M. Fleetwood, and J. D. Cressler, "Total ionizing dose effects on a high-voltage ($>30\text{V}$) complementary SiGe on SOI technology," *IEEE Transactions on Nuclear Science*, vol. 64, no. 1, pp. 277–284, Jan. 2017.
- [56] A. Wadsworth, *The Parametric Measurement Handbook*. Keysight Technologies, Dec. 2017.
- [57] J. D. Cressler and G. Niu, *Silicon-Germanium Heterojunction Bipolar Transistors*. Artech House, 2003.
- [58] H. Park and C.-K. K. Yang, "Nearly exact analytical formulation of the DNL yield of the digital-to-analog converter," *IEEE Trans. Circuits Syst. II*, vol. 59, no. 9, pp. 563–567, Sep. 2012.
- [59] B. S. Tolleson, P. C. Adell, B. Rax, H. J. Barnaby, A. Privat, X. Han, A. Mahmud, and I. Livingston, "Improved model for excess base current in irradiated lateral p-n-p bipolar junction transistors," *IEEE Trans. Nucl. Sci.*, vol. 65, no. 8, pp. 1488–1495, Aug. 2018.
- [60] L. Li, X.-C. Chen, Y. Jian, Z.-h. Li, Y.-z. Wu, J.-p. Zhang, M. Ren, B. Zhang, X.-L. Wu, Y.-l. Pang, and G.-x. Yang, "Improved model for ionization-induced surface recombination current in p-n-p BJTs," *IEEE Trans. Nucl. Sci.*, vol. 67, no. 8, pp. 1826–1834, Aug. 2020.
- [61] D. M. Fleetwood, "Total-ionizing-dose effects, border traps, and $1/f$ noise in emerging MOS technologies," *IEEE Trans. Nucl. Sci.*, vol. 67, no. 7, pp. 1216–1240, Jul. 2020.
- [62] D. M. Fleetwood, "Fast and slow border traps in MOS devices," *IEEE Trans. Nucl. Sci.*, vol. 43, no. 3, pp. 779–786, Jun. 1996.
- [63] A. H. Johnston, R. T. Swimm, and D. O. Thorbourn, "Charge yield at low electric fields: Considerations for bipolar integrated circuits," *IEEE Trans. Nucl. Sci.*, vol. 60, no. 6, pp. 4488–4497, Dec. 2013.
- [64] R. Pierret, *Semiconductor Device Fundamentals*. Addison-Wesley, 1996.
- [65] G. S. May and C. J. Spanos, *Fundamentals of Semiconductor Manufacturing and Process Control*. John Wiley & Sons, Inc., 2006.
- [66] Y. Gobert, P. Tasker, and K. Bachem, "A physical, yet simple, small-signal equivalent circuit for the heterojunction bipolar transistor," *IEEE Trans. Microw. Theory Techn.*, vol. 45, no. 1, pp. 149–153, Jan. 1997.

- [67] https://www.cadence.com/en_US/home/tools/custom-ic-analog-rf-design/layout-design/virtuoso-layout-suite.html, Accessed: Nov. 14, 2020.
- [68] J.-H. Tsai and C.-L. Lin, "A 40-GHz 4-bit digitally controlled VGA with low phase variation using 65-nm CMOS process," *IEEE Microw. Wireless Compon. Lett.*, vol. 29, no. 11, pp. 729–732, Nov. 2019.
- [69] V. Asgari and L. Belostotski, "Wideband 28-nm CMOS variable-gain amplifier," *IEEE Trans. Circuits Syst. I*, 2019.
- [70] Y.-T. Chang and H.-C. Lu, "A V-band low-power digital variable-gain low-noise amplifier using current-reused technique with stable matching and maintained OP1db," *IEEE Trans. Microw. Theory Techn.*, vol. 67, no. 11, pp. 4404–4417, Nov. 2019.
- [71] EMX, [ONLINE] Available: https://www.cadence.com/en_US/home/tools/system-analysis/em-solver/emx-planar-3d-simulator.html.
- [72] S. Seth, L. Najafizadeh, and J. D. Cressler, "On the RF properties of weakly saturated SiGe HBTs and their potential use in ultralow-voltage circuits," *IEEE Electron Device Lett.*, vol. 32, no. 1, pp. 3–5, Jan. 2011.
- [73] F. Inanlou, C. T. Coen, and J. D. Cressler, "A 1.0 V, 10–22 GHz, 4 mW LNA utilizing weakly saturated SiGe HBTs for single-chip, low-power, remote sensing applications," *IEEE Microw. Wireless Compon. Lett.*, vol. 24, no. 12, pp. 890–892, Dec. 2014.
- [74] M. Koolen, J. Geelen, and M. Versleijen, "An improved de-embedding technique for on-wafer high-frequency characterization," in *Proc. 1991 Bipolar Circuits and Technol. Meeting (BCTM)*, IEEE, Sep. 1991.
- [75] Z. Jiang, L. Zhang, Z. Liu, Z. Chen, H. Liu, Y. Wu, C. Zhao, and K. Kang, "A 33.5–39 GHz 5-bit variable gain LNA with 4 dB NF and low phase shift," in *2017 IEEE Asia-Pacific Microw. Conf. (APMC)*, IEEE, Nov. 2017.
- [76] B.-W. Min and G. M. Rebeiz, "Ka-band SiGe HBT low phase imbalance differential 3-bit variable gain LNA," *IEEE Microw. Wireless Compon. Lett.*, vol. 18, no. 4, pp. 272–274, Apr. 2008.
- [77] P.-H. Lo, C.-C. Lin, H.-C. Kuo, and H.-R. Chuang, "A Ka-band CMOS low-phase-variation variable gain amplifier with good matching capacity," in *2012 42nd Eur. Microw. Conf. (EuMC)*, IEEE, Oct. 2012.
- [78] S. Lee, J. Park, and S. Hong, "A Ka-band phase-compensated variable-gain CMOS low-noise amplifier," *IEEE Microw. Wireless Compon. Lett.*, vol. 29, no. 2, pp. 131–133, Feb. 2019.

- [79] Y.-T. Chang, Y.-N. Chen, and H.-C. Lu, “A 38 GHz low power variable gain LNA using PMOS current-steering device and gm-boost technique,” in *2018 Asia-Pacific Microw. Conf. (APMC)*, IEEE, Nov. 2018.
- [80] O. Adeniran, “A 27GHz-to-33GHz variable-gain amplifier with precise 0.5dB step size in 40nm-CMOS for 5G and Ka-band satellite applications,” in *2020 IEEE Int. Symp. on Circuits and Syst. (ISCAS)*, IEEE, Oct. 2020.